

(Univ. Prof. Dr. Friedrich Aumayr)



DIPLOMARBEIT

ELEKTRA - Electrostatic analyser measurements of ion transmission through thin free-standing foils

Ausgeführt am Institut für
Angewandte Physik
der Technischen Universität Wien
Wiedner Hauptstraße 8-10 / 134
1040 Wien

unter der Anleitung von

Univ.-Ass. Dipl.-Ing. Elisabeth GRUBER
Univ.-Prof. Dr. Friedrich AUMAYR

durch

Valerie SMEJKAL
Matrikelnummer 0826364
Hernalser Gürtel 2/35
1080 Wien

Wien, 22. Jänner 2016

Valerie Smejkal

Abstract

In the course of this masters thesis, charge loss and energy loss of ions in different charge states after transmission through atomically thin free-standing foils have been investigated. For this reason, an experiment was set up, analysed and taken into operation at the Institute of Applied Physics at TU Wien. As well as that, a series of measurements was performed at the Helmholtz-Zentrum Dresden-Rossendorf.

The interaction of ions with bulk materials is generally described using an equilibrium charge state of the projectile which is established after a few nanometres inside the solid due to electron loss and gain processes. Effects of pre-surface interaction can be neglected in this description.

The situation changes when the layer thickness is reduced to just a few atomic layers: pre-surface interactions may contribute measurably to the energy and charge change of the projectile. Additionally, the limited interaction time inside the material prohibits the establishment of an equilibrium charge state. Measurements of energy loss and charge loss of an ion after transmission through thin free-standing foils thus allows for a direct determination of fundamental processes governing the ion-condensed matter interaction.

The theoretical concepts of ion-surface and ion-condensed matter interaction are discussed in the first part of this thesis. Part two describes the experimental setups in Vienna and in Dresden, focusing on the electronics and the remote control of the experiment in Vienna that were installed in the course of this thesis. After that, simulations performed in SIMION, details on the commissioning of the setup and on the evaluation of the data are discussed. In the last part, preliminary results of the measurements are presented together with an outlook on further investigations.

Kurzfassung

Die hier verfasste Masterarbeit befasst sich mit der Vermessung von Ladungsverlust und Energieverlust von Ionen in verschiedenen Ladungszuständen nach Transmission durch dünne, frei stehende Schichten. Zu diesem Zweck wurde ein Experiment am Institut für Angewandte Physik der TU Wien aufgebaut, analysiert und in Betrieb genommen sowie eine Messzeit am Partnerexperiment am Helmholtz-Zentrum Dresden-Rossendorf verbracht.

Die Wechselwirkungen von Ionen mit herkömmlichen Festkörpern wird im Allgemeinen über einen Gleichgewichtsladungszustand, der sich nach wenigen Nanometern durch das Zusammenspiel von Elektronenverlust und Elektronenaufnahme einstellt, beschrieben. Effekte die vor der Oberfläche des Materials passieren, können hier vernachlässigt werden.

Verringert man nun die Schichtdicke auf wenige Atomlagen, so ändert sich die Situation: Wechselwirkungen, die vor der Oberfläche stattfinden können durchaus messbaren Einfluss auf die Energie- und die Ladungsänderung eines Projektils haben. Außerdem ist die Wechselwirkungszeit innerhalb des Materials zu gering, als dass sich ein Gleichgewichtsladungszustand einstellen könnte. Die Messung von Energieverlust und Ladungsverlust eines geladenen Projektils nach Transmission durch dünne freistehende Schichten ermöglicht somit eine direkte Messung fundamentaler Prozesse in der Ionen-Festkörper Wechselwirkung.

Im ersten Teil dieser Arbeit werden die theoretischen Grundlagen der Ionen-Oberflächen und der Teilchen-Festkörper Wechselwirkung beschrieben. Teil zwei widmet sich den experimentellen Anlagen in Wien und in Dresden. Der Schwerpunkt liegt auf der im Zuge dieser Arbeit installierten Elektronik und der Ansteuerung des Experiments in Wien. Danach werden Simulationen in SIMION, Details zur Inbetriebnahme des Experiments und zur Auswertung der Spektren diskutiert. Im letzten Teil finden sich die vorläufigen Resultate der Messungen sowie ein Ausblick auf zukünftige Projekte.

Contents

List of Acronyms	1
1 Motivation	2
1.1 Multiply charged ions in front of a surface	3
1.1.1 Metals	3
1.1.2 Insulating crystals	5
1.2 Interaction of particles with solids - the concept of stopping power .	6
1.2.1 Nuclear stopping	7
1.2.2 Electronic stopping	9
2 Experimental methods	10
2.1 The ion beam facility AUGUSTIN	10
2.1.1 Electronics	12
2.1.2 LabVIEW program	14
2.2 The Two-Source-Facility at HZDR	21
3 Analysis and operation of the setup	24
3.1 Pulse heights	24
3.2 Voltage offset and plasma potential	27
3.3 SIMION simulations	27
3.3.1 Peak shapes and widths	28
3.3.2 Angular shift of the peaks	31
3.4 Measurement procedure	34
3.5 Evaluation	36
3.5.1 Uncertainty estimation of the energy loss	38
4 Results	40
4.1 Discussion of the setup	40
4.1.1 Spectra	40
4.1.2 Offset voltage	41
4.1.3 Tilting angle of the analyser	43
4.2 Ar ^{q+} on CNM	43
4.3 Xe ^{q+} on single layer graphene	47

5	Summary and outlook	51
5.1	Summary	51
5.2	Outlook	52
	List of Figures	53
	List of Tables	54
	Bibliography	55
	Danksagung	

List of abbreviations

CMS	Centre of Mass System
CNM	Carbon Nano Membrane
COM	Classical Over the barrier Model
EBIT	Electron Beam Ion Trap
ECR	Electron Cyclotron Resonance
ELEKTRA	ELEKTRostatischer Analysator für Transmissionsmessungen an atomaren Folien
HA	Hollow Atom
HCI	Highly Charged Ion
HZDR	Helmholtz Zentrum Dresden Rossendorf
IAP	Institute of Applied Physics
MCP	MicroChannel Plate
SCPI	Standard Commands for Programmable Instruments
SOPHIE	SOURCE for Production of Highly charged Ions using Electron cyclotron resonance
TEM	Transmission Electron Microscopy

1 Motivation

Triggered by the development of the atomic theory at the beginning of the twentieth century, the interaction of particles carrying kinetic and potential energy with matter has inspired a considerable amount of experimental as well as theoretical work. The interaction of slow highly charged ions (HCI) has been a much researched topic in the last two decades. After intense research on HCI-surface interaction [1, 2] and theoretical modelling thereof [3–5], nanostructure formation by highly charged ions has been of great interest due to possible applications in nano-electronics [6] and medical applications [7]. Now with the possibility to produce increasingly thin films even in the form of one atomic layer, e.g. graphene [8], it is possible to directly access pre-equilibrium processes and gain an understanding which can ultimately help to tailor and manipulate the properties of these materials [9].

Collision studies between ions and free-standing thin membranes are also of fundamental interest since they bridge the gap between atomic collisions in gaseous and those in solid targets.

A collaboration between the Institute of Applied Physics (IAP) at TU Wien and the Helmholtz-Zentrum Dresden-Rossendorf (HZDR) recently lead to the observation of two distinct exit charge state distributions accompanied by a strong charge state dependent energy loss in transmission measurements of slow highly charged Xe ions through carbon nano membranes (CNM) of 1 nm thickness in an experiment at the HZDR [10]. A partner experiment, ELEKTRA, was designed at the IAP to extend the data to lower energy projectiles [11] and investigate different ion-target combinations.

In the following, an overview of the theoretical concepts concerning the interaction between highly charged ions and surfaces and particles with matter is given. Chapter 2 describes the experimental setups which were used for experiments. Chapter 3 focuses on the analysis of the ELEKTRA setup while chapter 4 describes the measurement and evaluation procedure. The results in chapter 5 are followed by a summary and an outlook.

Parts of the results of this thesis have meanwhile been submitted or are currently prepared for publication [12–14].

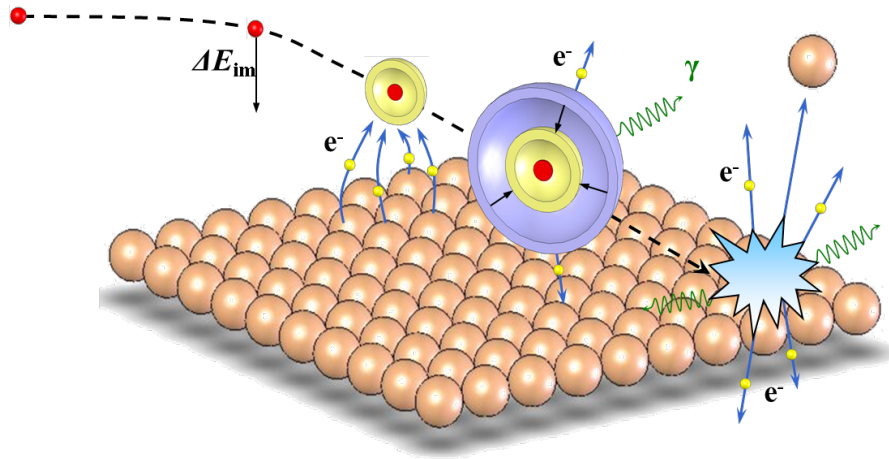


Figure 1.1: Image charge acceleration and hollow atom formation for a highly charged ion in front of a metal surface. This process is accompanied by Auger emission, followed by peel-off of the outer electrons upon entering the target and various sub-surface processes. Picture taken from [19].

1.1 Multiply charged ions in front of a surface

In this section, the interaction of multiply charged ions in front of a surface will be discussed. Following intense research and modelling of above surface processes like one electron capture [15] and multielectron transfer [16, 17] based on classical concepts, Burgdörfer, Lerner and Meyer [3] extended the classical over the barrier model (COM) to develop a comprehensive model of the neutralisation dynamics of highly charged ions in front of a metallic surface. The ideas presented in Section 1.1.1 are taken from their work unless stated otherwise. Later, this model was extended to insulating alkali halides by Hägg, Reinhold and Burgdörfer [5] as well as Ducree, Casali and Thumm [18].

1.1.1 Metals

In the classical over the barrier model [3] it is assumed that resonant transfer of electrons from the conduction band of a metal into highly excited states of an ion will take place as soon as the potential barrier between the surface and the projectile drops below the work function W_Φ of the material. It is supposed that the ion's velocity is far below the Fermi velocity of electrons inside the metal $v \ll v_F$ and the electrons in the conduction band are treated as a quasi-free electron gas. In front of a conducting surface, the active electron at position \vec{r} that is to be transferred to the ion is subject to a total potential energy that is the superposition of its own image potential energy $V_e^I(z)$, the interaction potential energy with the ion

$V_{pe}(|\vec{r} - R\hat{e}_z|)$ and the interaction energy with the ion's image potential $V_{pe}^I(\vec{r}, R\hat{e}_z)$,

$$V(z) = V_e^I(z) + V_{pe}(|\vec{r} - R\hat{e}_z|) + V_{pe}^I(\vec{r}, R\hat{e}_z) \quad , \quad (1.1)$$

where $z = \vec{r} \cdot \hat{e}_z$ is the electron's, R the ion's distance from the image plane and \hat{e}_z the direction of the surface normal. The electron image potential energy is given by

$$V_e^I(z) = -k \cdot \frac{e^2}{4(z + z_0)} \quad , \quad (1.2)$$

with the elementary charge e and where z_0 is a constant to make the potential continuous across the image plane. The prefactor k is defined by the unit system chosen for the calculations. The electron-ion interaction potential energy is given by the electrostatic potential energy with an effective charge

$$V_{pe}(|\vec{r} - R\hat{e}_z|) = -k \cdot \frac{q_{eff}(|\vec{r} - R\hat{e}_z|) \cdot e^2}{|\vec{r} - R\hat{e}_z|} \quad , \quad (1.3)$$

where $q_{eff}(|\vec{r} - R\hat{e}_z|)$ accounts for the screening of the ion's charge by its electrons during the surface approach. The ion image interaction potential energy takes into account the plasmon dispersion that is relevant close to the surface and evokes a screening of the polarisation [20]

$$V_{pe}^I(\vec{r}, R\hat{e}_z) = q \cdot e^2 \cdot \omega_s^2 \int_0^\infty dp \frac{J_0(r_{||}p) e^{-p(z+R)}}{\omega_s^2 + \alpha p + \beta p^2 + p^4/4} \quad . \quad (1.4)$$

Here, ω_s is the surface plasmon frequency, p is the momentum, α and β are material constants and J_0 is the Bessel function of zeroth order.

Once the electron transfer starts at a critical distance [3]

$$R_c = \frac{ke^2}{2W_\Phi} \sqrt{8q + 2} \quad , \quad (1.5)$$

where W_Φ is the work function of the metal, many electrons will be captured into high Rydberg states while the interaction time is too short for Auger deexcitation to fill the inner shells of the ion. Thus a so-called hollow atom is created which will be stripped of its outer electrons upon surface impact (peel-off) and neutralised within the target, see Figure 1.1. A competing process to the neutralisation of the ion in front of the target will also take place, namely the resonant loss of electrons into unoccupied states of the solid. Additionally, Auger ionisation will take place, thus re-ionising the projectile.

As the projectile approaches the surface, its energy levels will shift up and it will be subject to an accelerating force mediated by its image potential energy. The total energy gained due to this force has been determined to be in the order of [4]

$$\Delta E_{im} \approx \frac{W_\Phi}{3\sqrt{2}} + \mathcal{O}(q^{1/2}) \quad . \quad (1.6)$$

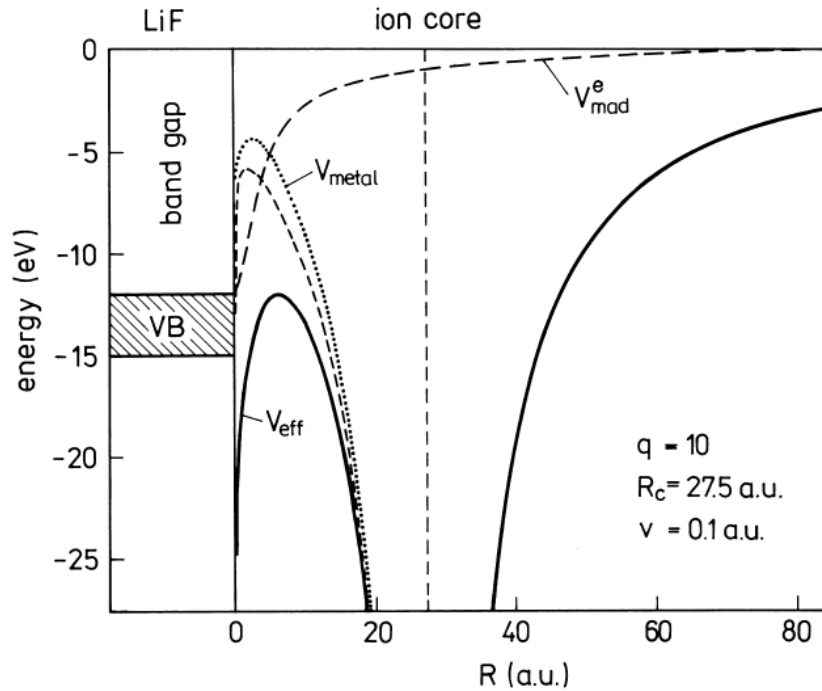


Figure 1.2: Interaction potentials for an ion with charge state $q = 10$ in front of a LiF surface. V_{eff} is the total potential energy governing the motion of an electron between the ion and the surface. Taken from [21].

1.1.2 Insulating crystals

When describing the interaction of a multiply charged ion with the insulating surface of an ionic crystal, several modifications have to be made to the single-electron potential energy described in Section 1.1.1. Due to its larger work function and the band gap, HCI-insulator-interaction can be expected to be quite different to the interaction of HCI with metals. The description given in the following will follow the model details given in [5], although the nature of the modifications is the same as in [18].

The potential energy governing the active electron's motion is extended by additional terms

$$V(z) = V_e^I(z) + V_{pe}(|\vec{r} - R\hat{e}_z|) + V_{pe}^I(\vec{r}, R\hat{e}_z) + V_{pol}(\vec{r}) + V_M(\vec{r}) + V_{sc}(\vec{r}) \quad . \quad (1.7)$$

An insulator, as opposed to a metal that can be modelled as a perfect conductor, will show a finite reaction to an external electric field. In linear response theory, this reaction is determined by its dielectric constant $\epsilon(\omega)$, which we have to take into account when calculating the self-image interaction potential energy of the active electron and the ion-image electron interaction potential energy. Here ω is the frequency of the perturbation and proportional to the absolute value of the

velocity of the ion $\omega \propto |v_z|$ for normal incidence. The adapted image potential energy contributions $V_e^I(z)$ and $V_{pe}^I(\vec{r}, R\hat{e}_z)$ are

$$V_e^I(z) \rightarrow \chi(z, z)V_e^I(z) \quad , \quad V_{pe}^I(\vec{r}, R\hat{e}_z) \rightarrow \chi(z, R\hat{e}_z)V_{pe}^I(\vec{r}, R\hat{e}_z) \quad , \quad (1.8)$$

where

$$\lim_{z, R\hat{e}_z \rightarrow \infty} \chi(z, R\hat{e}_z) = \frac{\epsilon(0) - 1}{\epsilon(0) + 1} \quad (1.9)$$

approaches 1 for a metal surface. The detailed expressions for the potential energy contributions in [5] have been omitted for clarity.

In addition to a modification of the potential energy terms already present in ion-metal interaction, the polarisation potential energy $V_{pol}(\vec{r})$ and the Madelung potential energy $V_M(\vec{r})$ representing effects coming from the crystal structure of the insulator are included into the total interaction potential energy. Finally, effects due to the local charge up of the surface after electron removal are included via a screening potential energy $V_{sc}(\vec{r})$. Within this model it is found that in ionic crystals, electron capture starts at closer distance than in metals, suppressing above surface neutral hollow atom formation which means that most of the potential energy is deposited in the bulk [22].

Measurements on the energy gain of highly charged ions in front of insulators surprisingly showed comparable results as in front of metallic surfaces for grazing incidence [23] while for normal incidence no image charge acceleration was found [24]. The existence of image charge acceleration for grazing incidence can be attributed to two counteracting effects: on the one hand, the neutralisation of the projectile is delayed due to the later onset of electron capture arising from higher binding energies and incomplete neutralisation. On the other hand, the different dielectric response of an insulator will diminish the image charge force. In normal incidence, the build up of localised charges on the surface counteracts the acceleration by the image charge.

1.2 Interaction of particles with solids - the concept of stopping power

From the first measurements of single particle scattering and the upcoming of the atomic model, the stopping of ions in various kinds of matter has been a widely researched topic. Since we attempt to investigate charge and energy loss of multiply charged ions in solids of limited thickness, the current concepts for stopping of ions in matter shall be reviewed briefly.

It is generally assumed that the energy loss of an ion in matter can be divided into two parts, the loss to the heavy target nuclei and the loss to the electronic system of the target, a distinction that was first suggested by Bohr in 1913 [27].

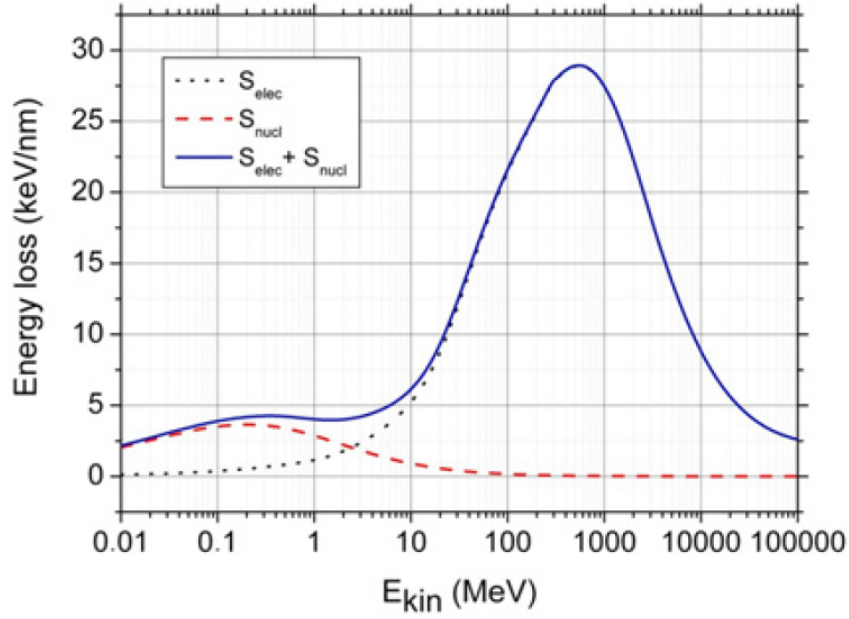


Figure 1.3: Energy loss contributions from nuclear and electronic stopping as a function of kinetic energy in MeV, calculated with the SRIM [25] code for the irradiation of SrTiO₃ with Xe ions. While nuclear stopping is large for small energies, electronic stopping predominates in high energy stopping. Taken from [26].

The justification for this separation lies in the fact that the light electrons move so fast that they can adapt to the movement of the slowly recoiling target atoms. The contribution to the overall stopping from nuclear or electronic stopping in the different energy regimes can be seen in Figure 1.3. While nuclear stopping is large for small energies, electronic stopping predominates in high energy stopping.

1.2.1 Nuclear stopping

The energy loss of a particle to the target nuclei has been termed *nuclear stopping*. The established approach in calculating nuclear stopping is to regard it as a sequence of single binary scattering events [28]. Using classical considerations for a potential that only depends on the distance between the two target nuclei, general expressions on the scattering angle and the energy transferred in the collision can be derived.

$$\theta(p) = \pi - 2 \int_{r_{min}}^{\infty} \frac{p dr}{r^2 \left[1 - \frac{V(r)}{E_C} - \frac{p^2}{r^2} \right]^{1/2}} \quad (1.10)$$

is the scattering angle in the centre of mass system (CMS), p the impact parameter, E_C the initial CMS energy and $V(r)$ the scattering potential. The distance of closest

approach r_{min} can be calculated by setting the denominator to zero

$$\sqrt{1 - \frac{V(r_{min})}{E_C} - \frac{p^2}{r_{min}^2}} = 0 \quad . \quad (1.11)$$

The expression for the transferred energy is

$$T(p, E_C) = \frac{4E_C M_C}{M_t} \sin^2 \frac{\theta(p)}{2} \quad , \quad (1.12)$$

where M_C is the reduced mass and M_t the mass of the target atom. The nuclear stopping cross section $S_n = \frac{1}{N} \frac{dE}{dx}$, where N is the atomic density of the target, can be obtained by integrating the transferred energy over all possible impact parameters

$$S_n = \int_0^\infty T(p, E_C) 2\pi p dp \quad . \quad (1.13)$$

The physics underlying a specific projectile-target combination enters via the not yet specified interaction potential $V(r)$. This potential consists of various contributions: for one there is the Coulomb interaction between the two nuclei, the interaction between the two electron distributions and the interaction of nuclei with the electron distribution of the other nucleus. For another there is an increase in kinetic energy due to Pauli excitation, where electrons have to occupy higher energy levels due to the Pauli exclusion principle when the electron clouds overlap and a contribution from the local change in electron density named exchange energy [25]. Taking all those contribution into account is a tedious task, so various attempts have been made to simplify the situation. The simplification is done by assuming a screened Coulomb potential as the scattering potential $V(r)$ which is then given by

$$V(r) = k \cdot \Phi(r/a_S) \frac{Z_1 Z_2 e^2}{r} \quad , \quad (1.14)$$

where Z_1 and Z_2 are the atomic numbers of the nuclei, r is the interatomic distance and $\Phi(r)$ is the screening potential with the screening length a_S . A lot of work has been done to determine the correct interatomic potentials and the length-scale on which they are screened, most prominently by Bohr in 1948 [29], Firsov in 1957 [30], Lindhard, Nielsen and Scharff in 1968 [31] and Ziegler, Biersack and Littmark in 1985 [28] who by comparison with experimental data found the so far most accurate, so-called *universal screening function*

$$\begin{aligned} \Phi_U(r/a_U) = & 0.1818 \cdot e^{-3.2r/a_U} + 0.5099 \cdot e^{-0.9423r/a_U} \\ & + 0.2802 \cdot e^{-0.4028r/a_U} + 0.02817 \cdot e^{-0.2016r/a_U} \quad , \end{aligned} \quad (1.15)$$

where $a_U = \frac{0.8853a_0}{(Z_1^{0.23} + Z_2^{0.23})}$ is the screening length obtained from experimental data.

In the above description the projectile and target are assumed to be neutral. To account for ionic charge states it was suggested to take the ion charge q instead of the atomic number Z_1 in distant collisions [32].

1.2.2 Electronic stopping

The energy loss to the electronic system of the target, which becomes dominant at high ion velocities, is known by the term *electronic stopping*. While the interaction of relativistic particles with matter can be described by point charges with the unscreened charge of the nucleus [33, 34], the screening of the nucleus by its surrounding electrons has to be taken into account when investigating ions at modest energies. Upon entering a target, a subsequent electron capture and loss process will lead to an equilibrium charge state of the projectile below the surface. The simplest estimate of the equilibrium charge state is given by the Bohr criterion that assumes that all electrons with orbital velocities less than the ion velocity are lost inside the medium [29]

$$\langle q \rangle = \frac{v}{v_0} Z^{1/3} \quad . \quad (1.16)$$

Here $v_0 = c \cdot \alpha_f \approx 2.19 \cdot 10^6$ m/s is the Bohr velocity (where α_f is the fine-structure constant) and Z the atomic number of the projectile. For the velocity regime $v \lesssim v_0$ two different theoretical approaches were developed almost simultaneously. Firsov [35] regarded the projectile-target collision system as a quasi-molecule with a flow of electrons between the overlapping electronic spheres of the collision partners, which he regarded as Thomas-Fermi atoms. The electron current transfers a netto momentum to the collision partners, connecting the energy loss to the number of particles transferred in the collision. Lindhard and Scharff [36] modelled this problem by regarding the momentum transfer to a uniform electron gas where the electrons have a slight drift velocity relative to the ion. Despite the different approaches, both theories arrive at a velocity dependent energy loss for low velocity heavy ions

$$\Delta E \propto v \quad . \quad (1.17)$$

It is known that highly charged ions that transverse foils of a few nanometers show an enhanced stopping [37–39] which has been attributed to larger stopping power before the ion reaches charge equilibrium. An attempt to explain this effect theoretically was made by Biersack [40] who predicts an increase in nuclear stopping proportional to q^2 .

2 Experimental methods

Energy and charge loss investigations were performed at the ion beam facility AUGUSTIN at the Institute for Applied Physics at TU Wien as well as at the Helmholtz-Zentrum Dresden-Rossendorf. In the course of this thesis, the setup at TU Wien described in [11] was completed and measurements on the interaction of Ar ions at energies of some keV with carbon nano membranes were performed. The measurements that were carried out at HZDR focused on the interaction of highly charged Xe ions at energies of some tens of keV with graphene.

The following chapter will give an overview of the two ion beam facilities and focus on the extensions that were made to the setup in Vienna.

2.1 The ion beam facility AUGUSTIN

The centrepiece of the ion beam facility AUGUSTIN at TU Wien (for a sketch see Figure 2.1) is the 14.5 GHz electron cyclotron resonance ion source SOPHIE - **S**ource for **P**roduction of **H**ighly charged **I**ons using **E**lectron cyclotron resonance. The operational principle of this type of ion source is to ionise gas atoms by multiple collisions with hot electrons. The thereby created plasma is heated via resonant absorption of microwaves by the electrons of the plasma (electron cyclotron resonance) and confined in a so-called "minimum-B" field structure. In this field structure, the magnetic field strength increases from the centre of the structure in every direction, thus mirroring particle velocities and trapping them. In the SOPHIE ion source, this field configuration is achieved by the superposition of an axial mirror field, provided by two radially and two axially magnetised rings, and a radial field created by a Halbach type hexapole magnet. This source is capable of producing Ar ions in charge states up to Ar^{14+} [41]. A detailed description of the ion source is found in [42]. After the ions are extracted from the source, two quadrupole magnets can be used to focus the beam and a sector magnet guides the ion beam into the experimental chambers and selects the $\frac{q}{m}$ fraction of the particles.

A cross section through beamline 1, housing the experimental setup used for thin foil transmission measurements, can be seen in Figure 2.2. The beam is collimated in the first section of the beamline, before it enters the target chamber. Figure 2.3 shows the details of the ion optical system. It consists of 4 apertures which can be used for current monitoring (aperture 4 is grounded) and 4 sets of deflection plates

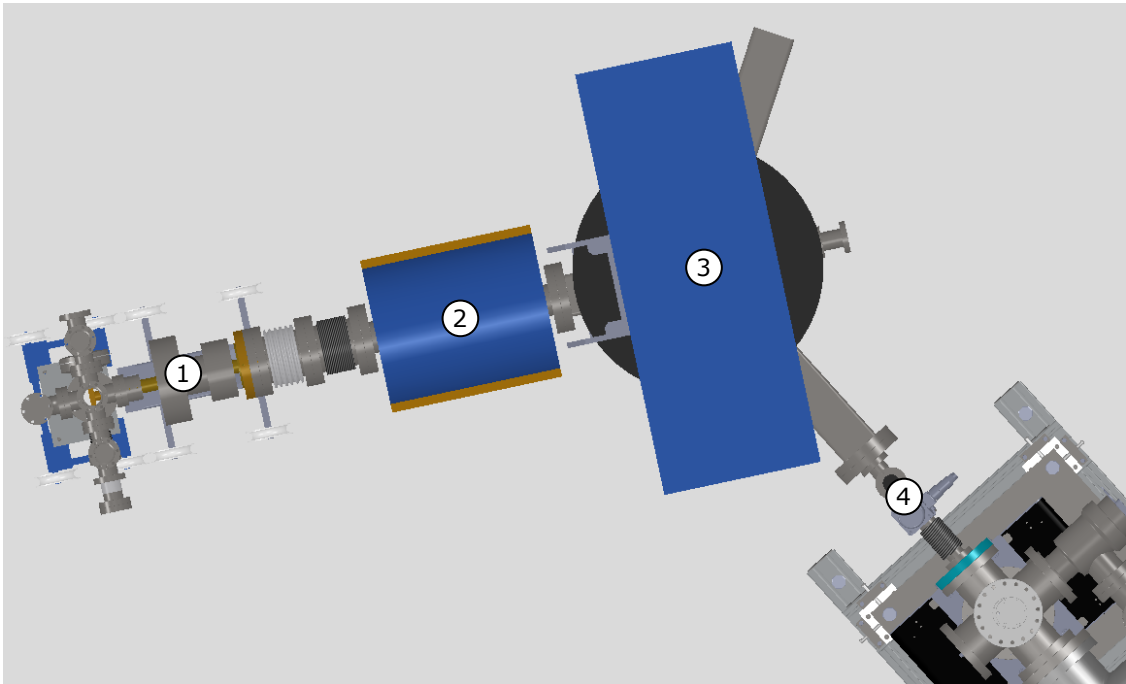


Figure 2.1: Sketch of the ion beam facility AUGUSTIN. ① The electron cyclotron resonance ion source SOPHIE. ② The quadrupole magnets. ③ The sector magnet. ④ The shutter to beamline 1.

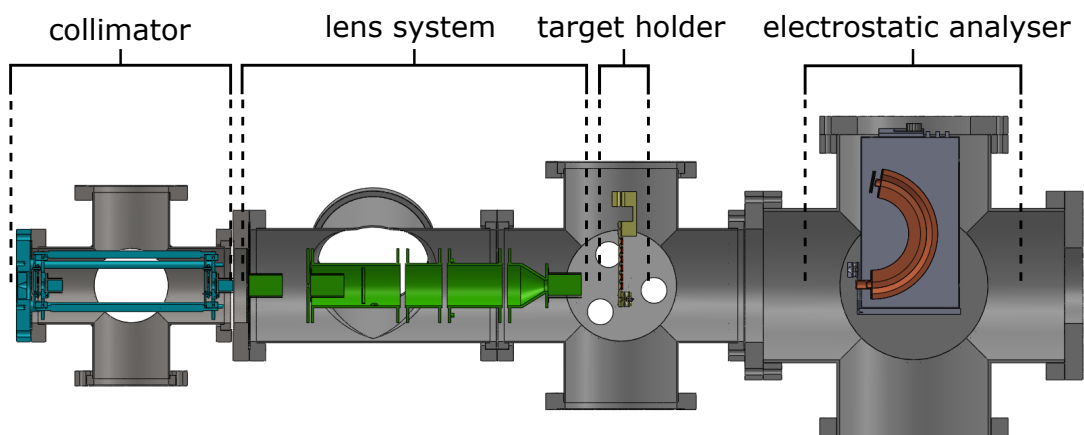


Figure 2.2: A cross section through the experimental setup. The collimator and the ion optical system are connected to the target chamber which is next to the chamber housing the electrostatic analyser.

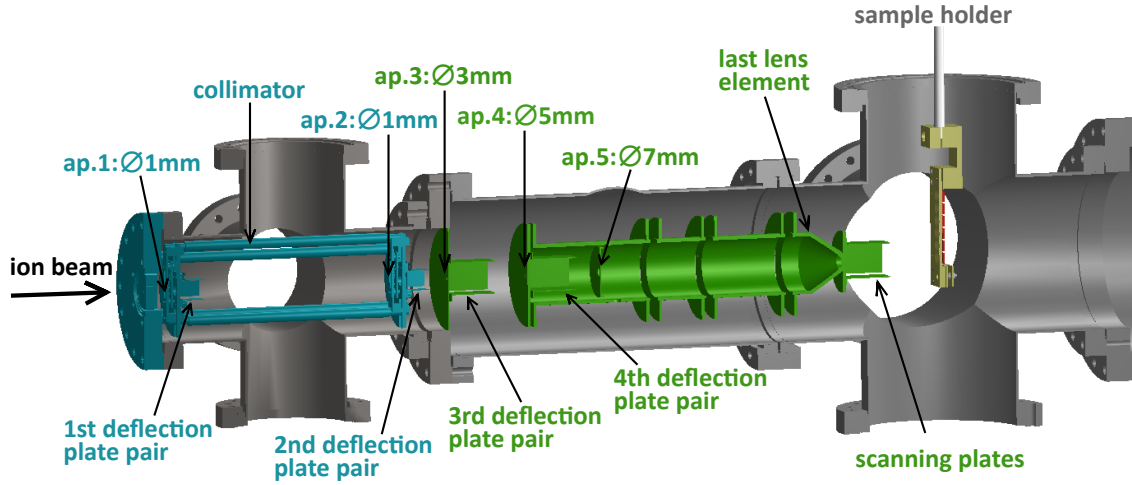


Figure 2.3: The collimator and the ion optics at the entrance of the beamline. Aperture 1-3 and the last lens element can be used to monitor the beam.

that are used for guiding the ion beam into the target chamber. For a detailed description of the collimator see [43].

After being guided through this first section of the beamline, the beam hits the target that is mounted on a rotatable holder that can hold multiple samples before it is detected by a spherical sector analyser that is mounted on a 4-axis-manipulator. Due to the distance between the target holder and the electrostatic analyser, the angular acceptance of the setup is limited to $\approx \pm 0.34^\circ$. The pass energy of this analyser is given by

$$U = \frac{E_{kin}}{q_{ion} \cdot g}, \quad g = \left(\frac{r_2}{r_1} - \frac{r_1}{r_2} \right)^{-1}, \quad (2.1)$$

where r_2 and r_1 are the radii of the outer/inner electrode respectively, see Equation 3.8. Its energy resolution is

$$\frac{\Delta E}{E} = 6.8 \cdot 10^{-3} \quad . \quad (2.2)$$

The carbon nano membranes that were used for transmission measurements were purchased from CNM Technologies, Bielefeld, Germany. The membranes are created by low energy electron irradiation leading to cross-linking of a self-assembled monolayer of aromatic molecules (1,1'-biphenyl-4-thiol) grown on a Au substrate. They are suspended on a lacey carbon film on a copper TEM grid with a mesh width of $60 \mu\text{m}$ and have a thickness of 1 nm [44].

2.1.1 Electronics

Since voltages of some kV are applied to the channelplate detector and the side plates of the electrostatic analyser, Kapton insulated coaxial cables with a DC

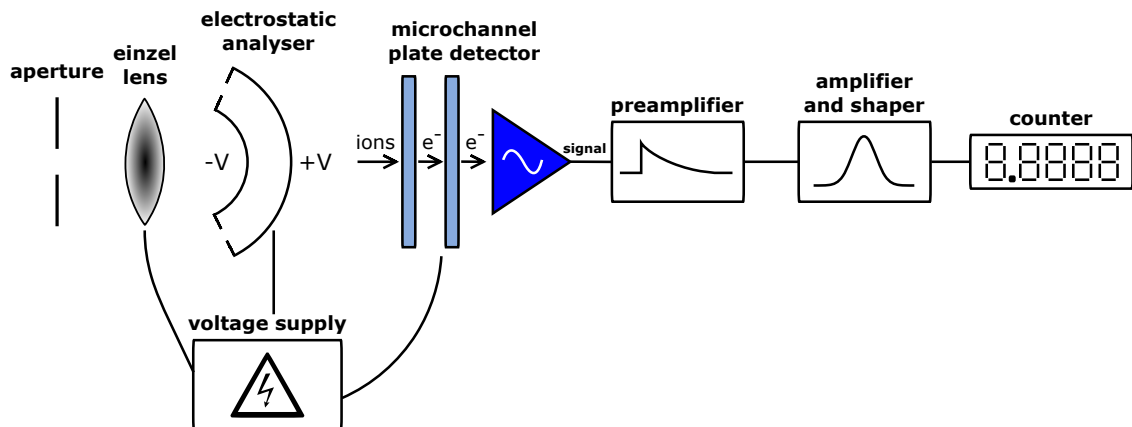


Figure 2.4: A schematic of the electronics used in the setup.

voltage rating of 10kV are used for most of the wiring inside the vacuum vessel. A solid Kapton insulated wire is used for the low voltage wiring.

Figure 2.4 shows a schematic of the electronics of the setup. An electrostatic three-element lens is positioned before the entrance slit of the analyser. The beam facing side of it acts as an aperture and the lens can be used to focus the incoming beam. In order to avoid a distortion of the energy loss peaks by the energy dependent focusing of such an electrostatic lens, the measurements were conducted with all lens elements grounded.

The electrostatic analyser plates are connected to the high stability, low noise, NIM crate powered modular voltage supply *NHS 6060x-K1* via coaxial cables with SHV (save high voltage) connectors. The assignment of the channels and the according reference inside the analyser are shown in Figure 2.5. The first three channels supply a positive voltage while the last three supply a negative one.

Ions that have the right energy to be focused onto the exit slit of the electrostatic analyser are detected by a set of microchannel plate (MCP) detectors model *comstock CP-602B*.

The thereby created signal is extracted from the MCP detector using a charge sensitive preamplifier *ORTEC 142B* that is located in close proximity to the signal output to minimise noise. Further processing of the signal, like shaping and amplification, is performed by the NIM BIN module amplifier *ORTEC 570*.

The *53131A 225 MHz Universal Frequency Counter/Timer* counts the signals above a certain threshold and sends them to the measuring computer via an RS232 interface.

A NIM BIN module ratemeter *ORTEC 661* is also part of the setup and can be used to visually monitor fast changes in the measured intensity during the optimisation of the beam alignment.

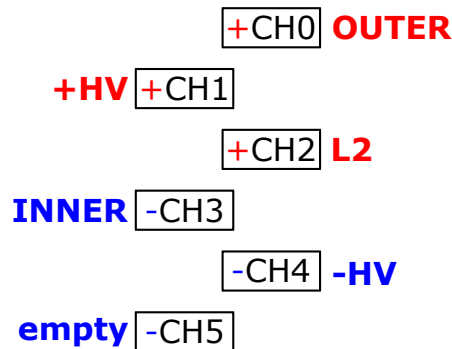


Figure 2.5: Channel layout of the voltage supply. The upper three channels supply a positive output voltage, the lower three a negative one. The outer and inner electrode of the electrostatic analyser are connected to OUTER and INNER respectively. The microchannel plate detector is connected to the +HV and -HV channels, where one of the two is left on ground potential. L2 marks the output channel for the einzel lens at the entrance of the analyser.

2.1.2 LabVIEW program

The following section contains a short description of the LabVIEW program designed for controlling the data acquisition of the experiment. The communication with the devices will be discussed first, before the description of the main program.

Communication with the voltage supply NHS 6060x-K1

The NHS 6060x-K1 voltage supply is equipped with a USB interface and can be controlled using Standard Commands for Programmable Instruments (SCPI). After driver installation, the communication with the device is quite straightforward and can be done using standard LabVIEW elements. The SCPI commands are terminated with a platform dependent end-of-line value and written to the COM-port specified by the *VISA resource name in* field. The voltage supply then echoes the command and the echo is read out. Before this repeated readout of the device, a wait-time of 250 ms is inserted to provide enough time for all of the response bits to be sent. A timeout can be set to ensure that the inner loop of the program terminates after a certain amount of time. A list of the commands used is found in Table 2.1.

Figure 2.6 shows the input and output nodes of the NHS_Commander.vi which implements the commands used during the measurement procedure. The *operation* node is used to specify the mode of operation. A list of the modes of operation of this VI is given in Table 2.2.

command	description
:VOLT_ON,(@<channel list>)	activate specified channels, e.g. (@1,3,5) or (1-5)
:VOLT_OFF,(@<channel list>)	deactivate specified channels
:VOLT_<Voltage>[V],(@<channel list>)	set voltage at specified channels
:READ:VOLT:ON?_(@<channel list>)	check if the channels are activated 0 = OFF, 1 = ON
:MEAS:VOLT?_(@<channel list>)	measure the output voltages at specified channels
:READ:VOLT?_(@<channel list>)	read out set voltages at specified channels
:CONF:RAMP:VOLT_<RampSpeed>[% V_{nom} /s]	set the ramp speed in percentage of the nominal voltage, which is $V_{nom} = 6000V$
:READ:RAMP:VOLT?	read the set voltage ramp speed
:MEAS:CURR?_(@<channel list>)	measure the output current at specified channels

Table 2.1: SCPI commands used in communicating with the voltage supply.

operation	description
1	Activate the channels specified in channel list.
2	Deactivate the channels specified in channel list.
3	Set the voltage ramp in % of V_{nom} /s.
4	Measure the voltages at all channels. Returns an array containing them.
5	Read the set voltages of all channels. Returns an array containing them.
6	Read out the set ramp speed.
7	Query the channel status of all channels. 0 = OFF, 1 = ON.
8	Measure the currents at all channels.

Table 2.2: Operational modes of the NHS_Commander.vi.

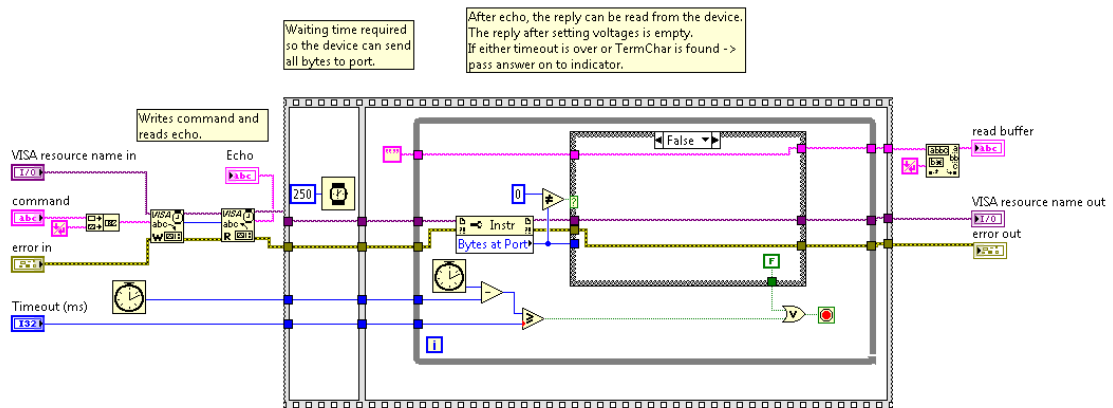


Figure 2.6: Block diagram of the sub-VI `NHS_ReadWrite.vi` for communication with the voltage supply. The voltage supply then echoes the command and after a wait-time of 250 ms the answer is read out. A timeout can be set to ensure that the inner loop of the program terminates after a certain amount of time.

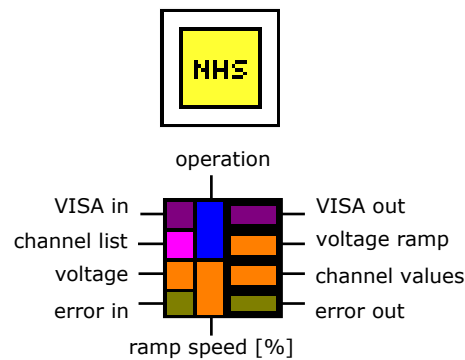


Figure 2.7: Symbol and inputs/outputs of the voltage supply control program `NHS_Commander.vi`.

Communication with the Agilent 53131A 225 MHz Universal Frequency Counter

The communication with the frequency counter required finding out the timing behaviour of the device. The serial settings (baud rate, parity bits, etc.) can be specified in the device menu and have to be set accordingly in the program `Read_5313X.vi`. An instrument timeout can be set within the program which, after expiration, terminates the data transmission. When communicating via RS232 (the other option would be GPIB), the counter writes the frequency/count information into a buffer whenever it is available and terminates it with an end-of-line constant. In order that only the latest information is read out, the buffer is emptied before each readout. Part I in Figure 2.8 shows the acquisition of the counter output. Any completely transmitted output number will be 17 bits long. The information is read

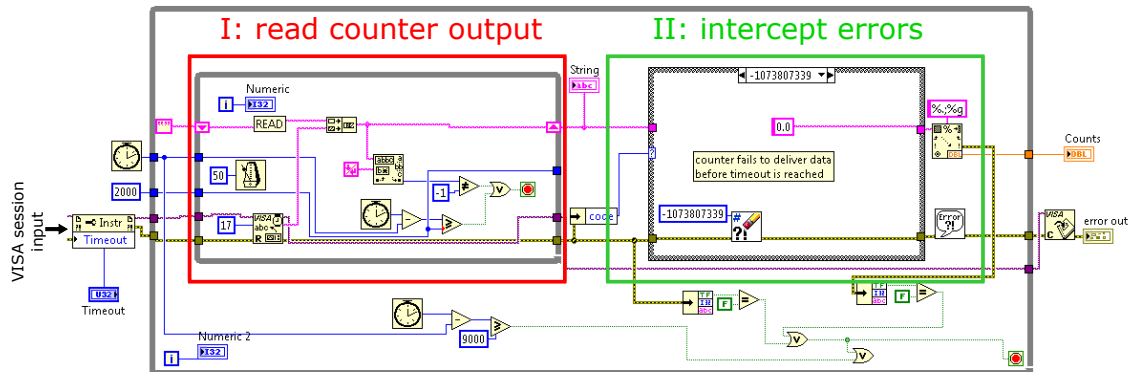


Figure 2.8: Block diagram of the counter readout. Part I (red) handles the readout of the data bits sent by the counter while part II intercepts frequent errors caused by damaged data bits or the session exceeding the timeout.

from the port until the terminating character is found, with a waiting time of 50 ms between each request. If no terminating character is sent, the loop will terminate after 2 seconds. Part II of the Read_5313X.vi, Figure 2.8, consists of an error handler, which intercepts two frequent errors that might occur. When measuring very low frequencies, which is the case when measuring at voltages where no ions can pass the set analyser voltage, the session will terminate without any information being sent. This invokes an error in the VISA-read which is detected and deleted before a frequency output of 0 is written to the read-buffer. The second case where interception is necessary comes up when a lot of information is transmitted by the device, like it happens for high count rates, and a framing error occurs.

The data comes in the format xxx,xxx,xxx.xxx MHz, so the commas are deleted and the resulting number string is then converted to a float.

Program for optimisation and main program

In the course of this thesis, two LabVIEW programs have been written to control the beam alignment (Elektra_Optimise.vi) and to record the spectra (Elektra_Main.vi) which are combined in the LabVIEW project Elektra.lvproj.

The front panel of the program for beam optimisation is displayed in Figure 2.9. By selecting the according tab, the user can choose between symmetric and independent control of the inner and the outer electrode. Symmetric control means that half of the typed in voltage is applied to both electrodes while with the independent control the user can apply arbitrary voltages to each electrode. The green squares on the right of the voltage displays indicate whether a channel is activated or not. The counter timeout determines how long the counter sub-VI waits for a signal, see Section 2.1.2. For displaying the incoming count rate there is a live graph on the bottom and a ratemeter on the right, which can be deactivated. On the right

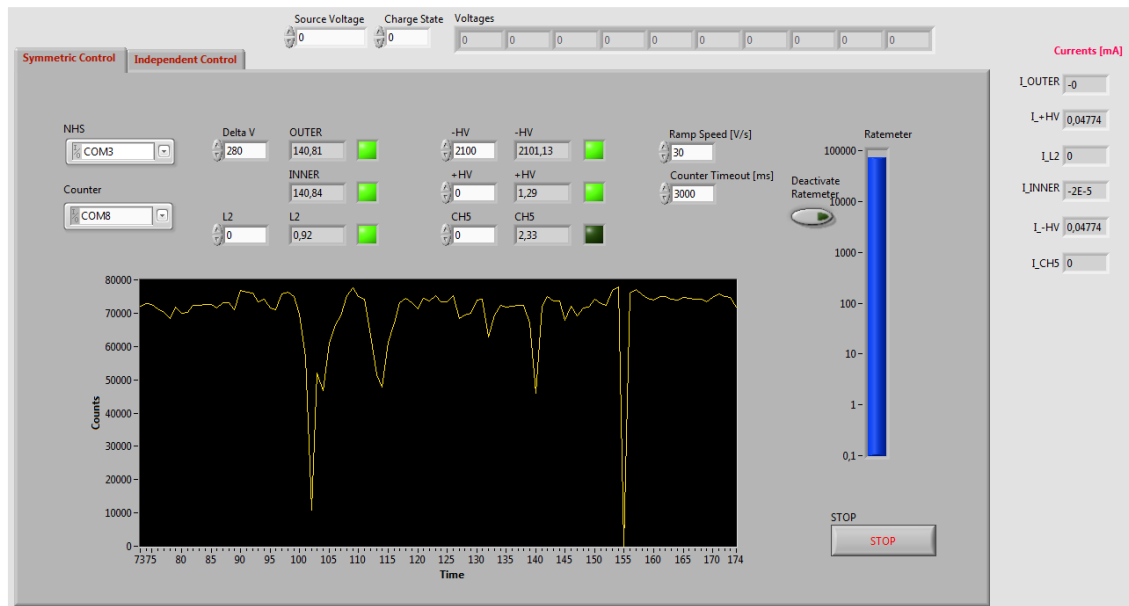


Figure 2.9: Main screen of the program for optimisation of the beam alignment.

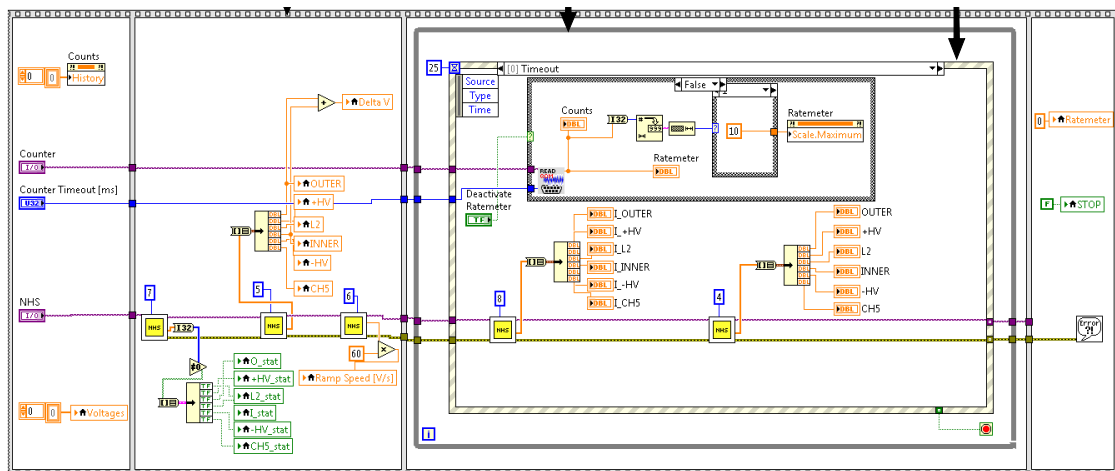


Figure 2.10: Block diagram of the program for beam optimisation. The first two sections of the flat sequence handle the communication with the devices and the acquisition of the initial values. The main part of the program is the event structure inside the while loop which will respond to value changes of the controls on the front panel.

there are indicators to monitor the current that flows through the channels of the NHS. When typing in the source voltage and the initial charge state of the ions, the expected voltage difference between the electrodes of the electrostatic analyser for decreasing charge states are displayed.

Figure 2.10 shows the block diagram of Elektra_Optimise.vi. The first two sections of the flat sequence handle the communication with the devices and the ac-



Figure 2.11: Main screen of the measurement program.

quisition of the initial values. The main part of the program is the event structure inside the while loop which will respond to value changes of the controls on the front panel. When nothing happens for 25 ms, the timeout event of the loop, which is updating the indicator values and readout of the counter, is executed.

When the beam is optimised, the main program `Elektra_Main.vi` can be used to record a spectrum, see Figure 2.11 for the front panel. The panel named *File Info* is used to save general information on target type, charge state and source voltage. There are two different recording regimes, the *On Peak* and the *Off Peak*, which can be set independently to abbreviate measurements by choosing different step widths. The field *Peak Scan Area* in the *General Settings* is used to state when the measurement enters one or the other regime by comparing the current voltage with the one calculated from the initial ion energy. Since the peaks are asymmetric, the peak scan area is shifted such that 3/4 of the scan area are below the supposed voltage and 1/4 is above. Another way to reduce the measuring time is to skip a voltage range where no peaks are expected using the *Skip Voltages* button. The block diagram is fairly easy to understand, so it will not be discussed. One thing

the user should always be aware of when handling the electrostatic analyser is that the maximum voltage difference between the two electrodes lies around 3000 V.

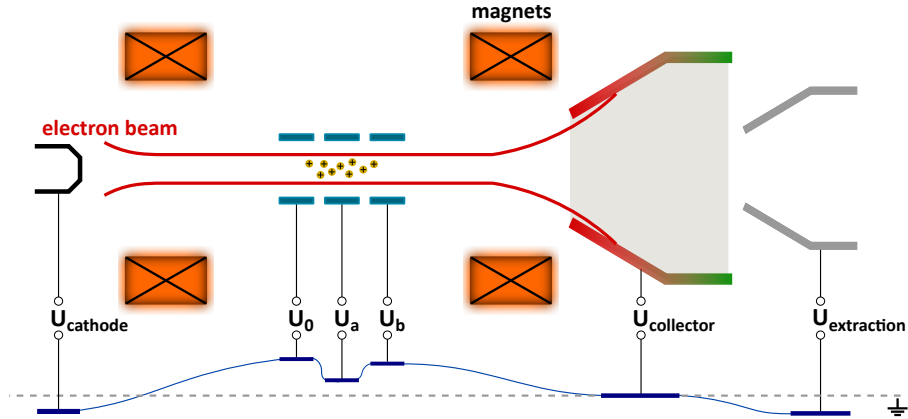


Figure 2.12: Working principle of an electron beam ion trap. An electron beam ionises the gas and induces radial trapping. The axial trapping is achieved by a potential well created by U_0 , U_a and U_b .

2.2 The Two-Source-Facility at HZDR

The Two-Source-Facility at HZDR is a combination of an ECR ion source and a room temperature EBIT (**E**lectron **B**eam **I**on **T**rap) [45, 46]. For the experiments described here, only the EBIT was used.

The working principle of an electron beam ion trap is to expose positive, electrostatically trapped ions to a magnetically compressed and quasi-monoenergetic electron beam launched from an electron gun. The radial trapping of the ions is achieved by the space charge of the electron beam while the axial trapping comes from biasing three drift tubes in such a way that a negative potential well is created. The working principle and the potentials inside an EBIT are sketched in Figure 2.12. There are two modes of operation of the EBIT, the leaky mode where the ions can escape continuously and the pulsed mode [47] which can be used for high intensity ion pulses. All results described were obtained using leaky mode. With the EBIT at HZDR, Xe ions in charge states up to 44+ can be created [45].

The ions leaving the potential well are accelerated over a voltage difference of 4400 V and $\frac{q}{m}$ -analysed with a sector magnet. Different beam energies are attained via electrostatic deceleration by biasing the potential of the beamline with respect to the target chamber.

Inside the target chamber, a target holder that can hold multiple targets is mounted on a 4-axis-manipulator followed by a cylindrical electrostatic analyser that is attached to a rotatable mounting. The detector used for ion detection is a channeltron electron multiplier. The angular acceptance of this setup is $\approx \pm 1.6^\circ$. The pass energy is given by

$$U = \frac{E_{kin}}{q_{ion} \cdot g}, \quad g = \left[\ln \left(\frac{r_2}{r_1} \right) \right]^{-1}, \quad (2.3)$$

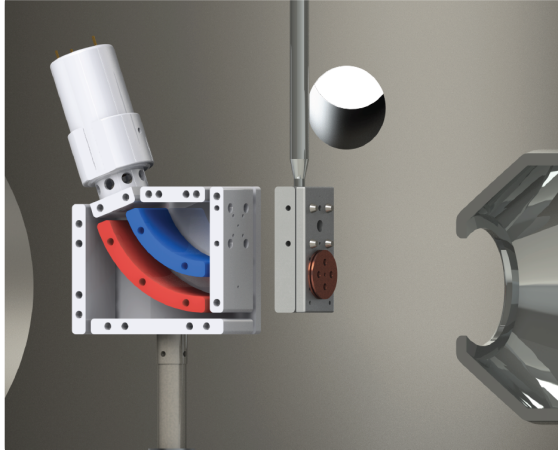


Figure 2.13: Target chamber of the setup at the HZDR. From right to left: the beam exit aperture, the target holder, the cylindrical electrostatic analyser with channeltron detector.

where r_2 and r_1 are the radii of the outer and the inner electrode respectively. Its energy resolution was measured to be

$$\frac{\Delta E}{E} \approx 1.5 \cdot 10^{-3} \quad . \quad (2.4)$$

The target used in experiments at the HZDR described in this thesis was a single layer graphene sheet suspended on a gold Quantifoil TEM grid.

It was produced by the AG Schleberger at the University Duisburg-Essen by chemical vapour deposition of graphene onto a Cu foil substrate. For isolating the graphene, the foil is wetted with isopropyl alcohol and a gold Quantifoil TEM grid is placed on top such that it is in complete contact with the graphene. The copper is then etched away using an ammonium persulfate solution. The ammonium persulfate solution is then neutralised with purified water and in a last step the TEM grid with the graphene is taken out to dry.

Figure 2.14 shows a TEM image of the graphene used for measurements. The regular structure from the honeycomb lattice is clearly visible. The irregular spots, which are contaminations, only cover a relatively small area.

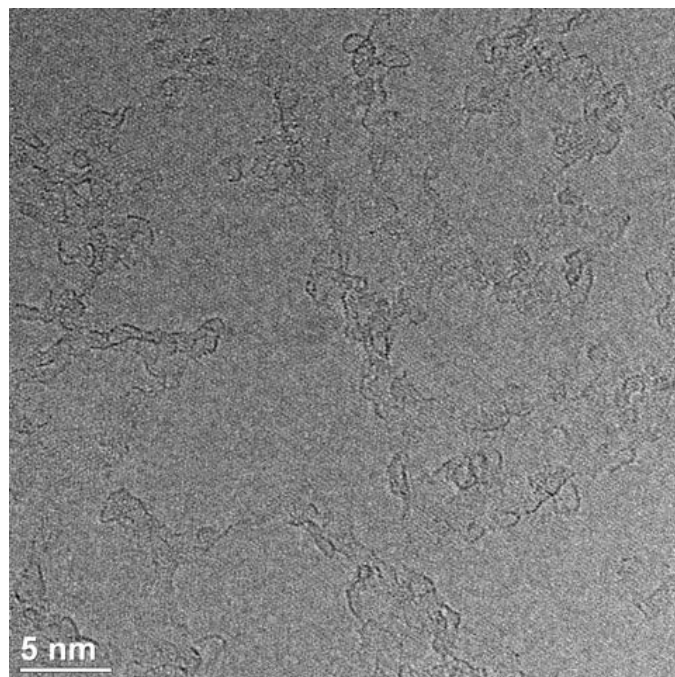


Figure 2.14: TEM image of the graphene sheet used in the experiments. The regular structure from the honeycomb lattice is clearly visible. The irregular spots are contaminations.

3 Analysis and operation of the setup

In order to obtain reliable results using the ELEKTRA setup, a thorough analysis of the system was performed which will be described in the following.

3.1 Pulse heights

For the detection of the incoming particles, a microchannel plate detector has been used. An MCP is a disk, usually made of lead glass, containing densely packed, parallel tubes with a diameter of 10-100 μm that are coated to have a high secondary electron emission coefficient and a certain resistivity, which then act as electron multipliers [48–50]. The working principle is as follows: an incident particle that hits the surface of the MCP will, with a certain probability, produce some secondary electrons. By applying a bias voltage between the two sides of the disc, the electrons are accelerated down the channels and produce an avalanche of secondary electrons along their way. This electron cloud can then be detected by an anode on the other side of the MCP.

To avoid the problem of ionic feedback, which will deteriorate the signal, the MCP detector used in this experiment is in the chevron configuration, see Figure 3.1c [51]. This configuration also allows for the application of higher bias voltages, thus higher gains and better single particle detection are obtained. Figure 3.1a shows the disk layout of an MCP with a cut view through the channel while Figure 3.1b visualises the working principle of the channel amplification.

Space charge saturation due to electrostatic repulsion within the electron cloud causes the gain to flatten with increasing voltage. When the MCP is not saturated, the output signal pulse height distribution will follow an exponential curve. In the region where space charge saturation is predominant, the pulse height distribution becomes peaked [50, 52]. This regime is ideal for particle counting, because the background noise and the signal induced by the particle can be well distinguished.

Part of a thorough analysis of the detection system thus is finding the optimal gain for the experiment that will enable us to efficiently detect all of the incoming particles. For this reason, the pulse height distributions for ions of different charge states at various bias voltages were taken using a *CAEN N957* multi channel analyser. The pulse height signal is binned with a bin separation of 1.22 mV, so each

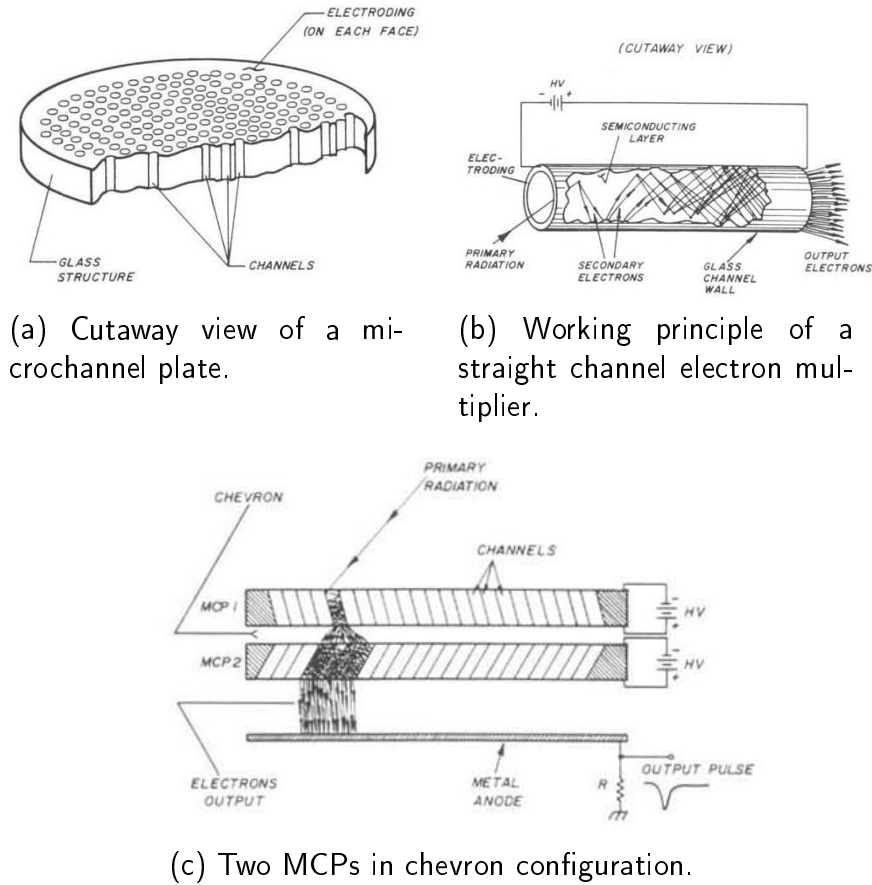


Figure 3.1: (a): the densely packed channels embedded in lead glass with conductive coating on both sides. (b): the working principle of one of these channels. A cloud of secondary electrons is created upon ion impact which is amplified along the channel. (c): a schematic of the chevron configuration. The channels of two MCPs are tilted against each other to avoid ionic feedback. Pictures taken from [48].

channel corresponds to a pulse height bin of 1.22 mV width. Figure 3.2 shows the charge state dependence of the peak height distribution for Ar^{q+} ions with q between 2 and 9, at kinetic energy of 25.9 keV, a bias to the detector of 2100 V and count rates around 3 kHz. The original data was fitted by the function

$$f(x) = A \cdot x \cdot e^{-x/\lambda} \quad (3.1)$$

to obtain the maximum. There is a slight shift to higher channels with increasing charge state. This can be attributed to a higher secondary electron emission upon impact of the charged particle on the MCP.

The analysis of the bias voltage dependence of the signal maximum position, e.g. the detection efficiency, is shown in Figure 3.3 for Ar^{9+} ions at a kinetic energy of 5.8 keV and count rates around 3 kHz. As expected, the distribution shifts towards

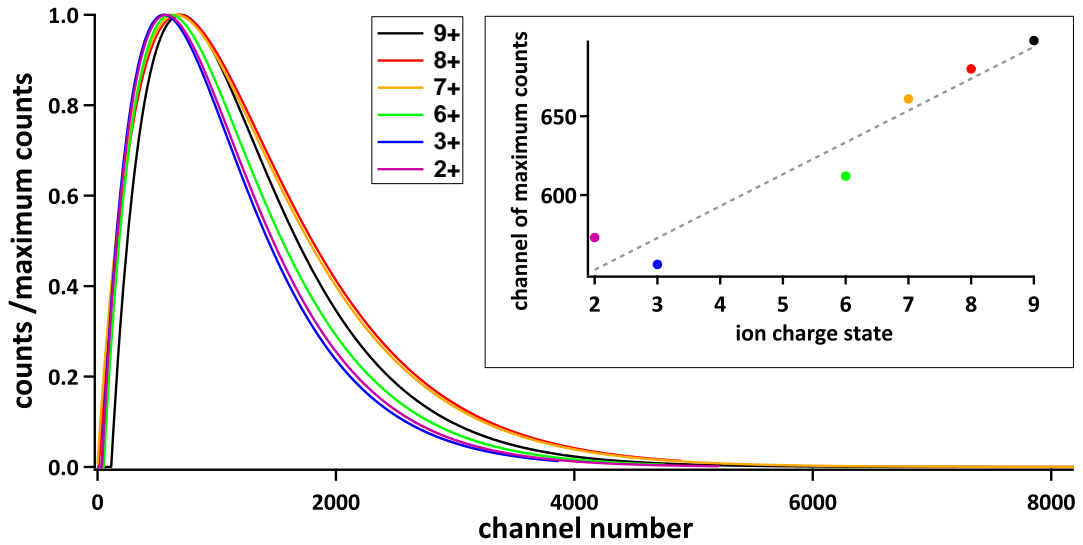


Figure 3.2: Analysis of the shift of the pulse amplitude distribution with different incident ion charge state. The curves are fits to the original data. The pulse height signal is binned with a bin separation of 1.22 mV, so each channel corresponds to a pulse height bin of 1.22 mV width. The subplot shows the maximum of the distribution over the incident charge state. The dashed grey line is there to guide the eye. All curves were taken at $E_{kin} = 25.9$ keV, count rates around 3 kHz and a detector bias of 2100 V.

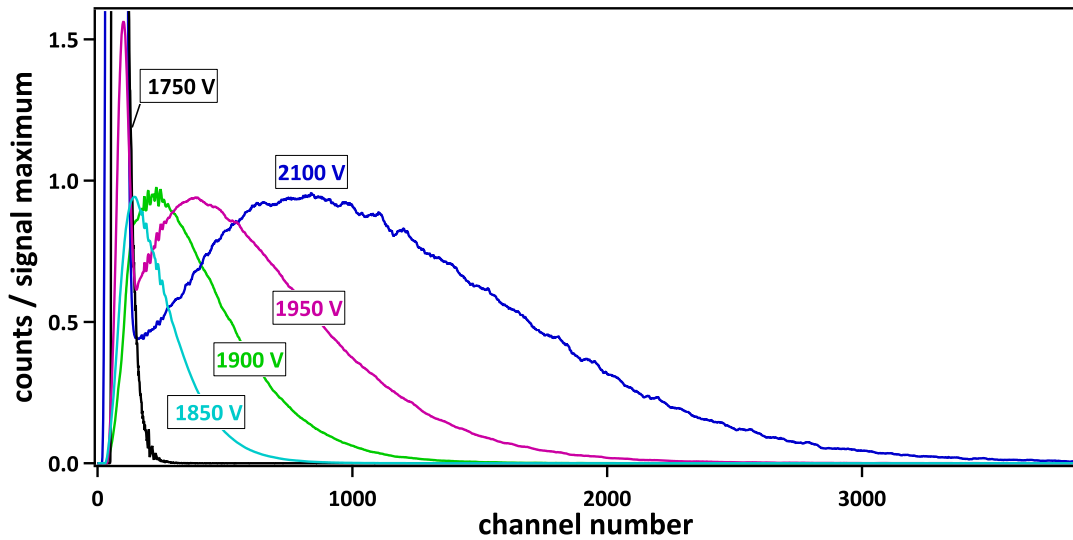


Figure 3.3: Analysis of the shift of the pulse amplitude distribution with different voltages applied to the detector. Again the pulse height signal is binned with a bin separation of 1.22 mV, so each channel corresponds to a pulse height bin of 1.22 mV width. The curves have been smoothed and are normalised to the signal maximum. The higher distribution at low channels can be attributed to noise. The oscillations around channel 200 are digitising errors. All curves were taken at $E_{kin} = 5.8$ keV and count rates around 3 kHz.

larger signal heights (higher channels) with higher bias voltage and is well separated from the low amplitude noise tail.

Based on the findings of the peak height analysis, the detector was operated at a bias of 2100 V.

3.2 Voltage offset and plasma potential

The use of an ECR ion source has the disadvantage that, due to higher electron mobilities, the potential of the plasma relative to the walls will be raised [53]. When the ions are extracted from the plasma chamber by an applied potential of U_{extr} , their final energy will actually be $q \cdot (U_{extr} + U_{plasma})$, thus slightly higher than the one specified by the source settings. Out of this reason, the initial energy of the ion beam needs to be determined from the position of the primary peaks of the spectra.

The accuracy of the determination strongly depends on the accuracy of the voltage readout of the NHS 6060x-K1 voltage supply. According to the technical specifications, the accuracy of the measured output voltage of the device is given by

$$\Delta U = \pm(2 \cdot 10^{-4} \cdot U_{nom} + 10^{-4} \cdot U_{out}) \quad , \quad (3.2)$$

where U_{nom} is the nominal voltage of the device (6000 V) and U_{out} is the actual output voltage. For the model used in the ELEKTRA-setup this means

$$\Delta U = \pm(1.2 \text{ V} + 10^{-4} \cdot U_{out}) \quad . \quad (3.3)$$

Since this intrinsic uncertainty leads to a substantial error in the determined initial energy especially for high charge states, see Equation 3.8, it is desirable to reduce this error. This is achieved by comparing the measured voltages from the device with more accurate external measurements. For this purpose, voltages in a range between 20 V and 400 V were measured using a *Fluke 83* multimeter. The results of these measurements are given in Table 3.1.

3.3 SIMION simulations

To further investigate the behaviour of the analysing system, simulations of the ion trajectories were performed using SIMION 8.0 [54]. In SIMION, charged particle optical systems are calculated via finite difference methods and Runge-Kutta is used for solving the required partial differential equations. A user program was created to scan the incoming beam and analyse changes of the output peak width, shape and position with input energy, charge state and angle. Figure 3.4 shows the model of the analyser together with the coordinate system used in the subsequent descriptions.

V_{set}	NHS	Fluke 83	offset	accuracy
20	20.05	20.7	- 0.65	0.030
30	30.04	30.7	- 0.66	0.040
50	50	50.7	- 0.7	0.15
100	100.1	100.68	- 0.58	0.20
120	120.1	120.7	- 0.6	0.22
140	140.1	140.7	- 0.6	0.24
160	160.1	160.72	- 0.62	0.26
180	180.13	180.7	- 0.57	0.28
200	200.2	200.72	- 0.52	0.30
220	220.2	220.75	- 0.55	0.32
240	240.2	240.72	- 0.52	0.34
260	260.2	260.75	- 0.55	0.36
280	280.3	280.75	- 0.45	0.38
300	300.3	300.78	- 0.48	0.40
320	320.3	320.75	- 0.45	0.42
340	340.3	340.77	- 0.47	0.44
360	360.3	360.76	- 0.46	0.46
380	380.4	380.8	- 0.4	0.48
400	400.3	400.75	- 0.45	0.50

Table 3.1: Voltage calibration: all values are given in volts. The first column shows the set voltage, the second the voltage read out from the device, the third the voltage measured with the more accurate Fluke 83 multimeter. Column four shows the difference between column two and three, while column five shows the absolute accuracy of the Fluke 83 for each voltage value in volts.

3.3.1 Peak shapes and widths

A crucial part when fitting the measured spectra is knowing the transfer (spectrometer) function $T(E, q)$ of the analyser, that is the shape and width of peaks created by a sharp, δ -shaped energy profile of the beam. Once this transfer function is known, the peak shape as observed in the measured spectra $\Phi(E, q)$ is obtained by convolving $T(E, q)$ with the energy profile of the beam $\phi(E)$. The transfer function will therefore, by influencing the mean of an asymmetric energy profile, influence the energy loss calculated from the spectra. It also broadens the peaks, thus affecting the integral and thereby the intensity calculated from the spectra via

$$\int \Phi(E, q)dE = \int (T * \phi)(E, q)dE = \int T(E, q)dE \cdot \int \phi(E)dE \quad . \quad (3.4)$$

In the following, analytical considerations on the transfer function are presented.

The electric field \vec{E} in radial direction created by applying a potential between

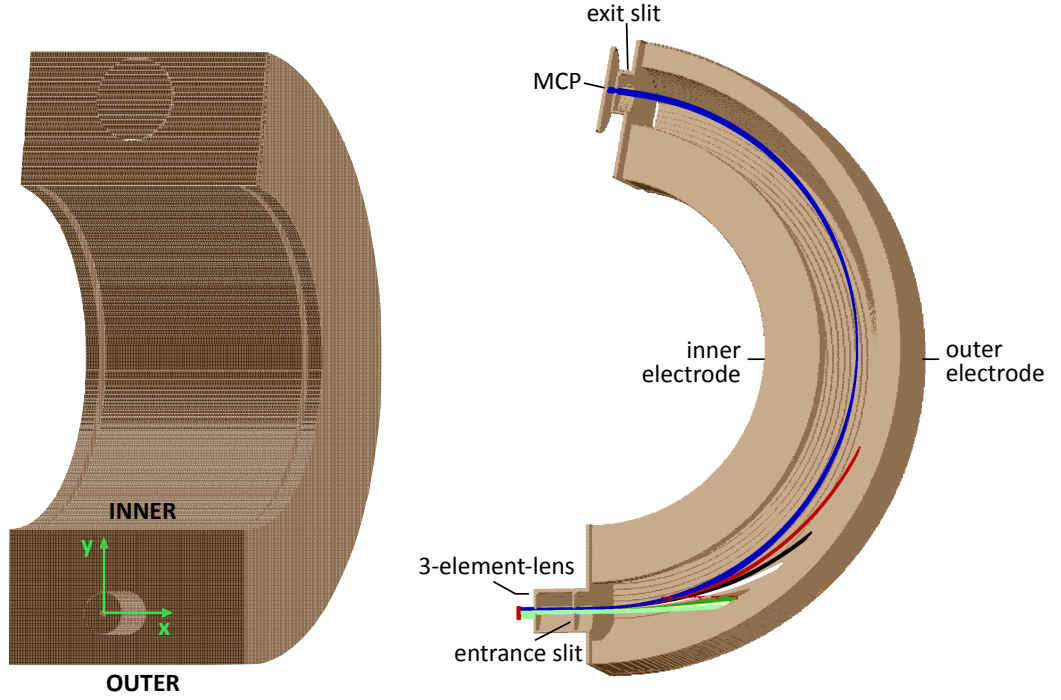


Figure 3.4: Simion model of the electrostatic analyser. Left: coordinate system used for description. Right: cut through the analyser with ion trajectories and labelling of the parts.

the analyser plates is given by

$$\vec{E} = \frac{Q}{4\pi\epsilon_0 r^2} \hat{r} \quad , \quad Q = C \cdot U \quad . \quad (3.5)$$

Here, Q is the charge that collects on the outer sphere when a potential difference of $U = U_{outer} - U_{inner}$ is applied between the outer and inner electrode and C is the capacitance which is given by

$$C = \frac{4\pi\epsilon_0}{\frac{1}{r_1} - \frac{1}{r_2}} \quad , \quad (3.6)$$

where r_1 and r_2 are the inner/outer radius respectively.

A particle entering this field will be forced to follow a curved trajectory. The voltage necessary for a particle of a given energy entering the analyser concentric to the entrance aperture and exiting it at the same radius (central trajectory) is easily calculated using by fact that in this case the centrifugal force just balances the central force provided by the voltage difference.

$$q_{ion} \cdot E(R) = q_{ion} \cdot \frac{C \cdot U}{4\pi\epsilon_0 R^2} = 2 \cdot \frac{E_{kin}}{R} \quad , \quad R = \frac{r_1 + r_2}{2} \quad , \quad (3.7)$$

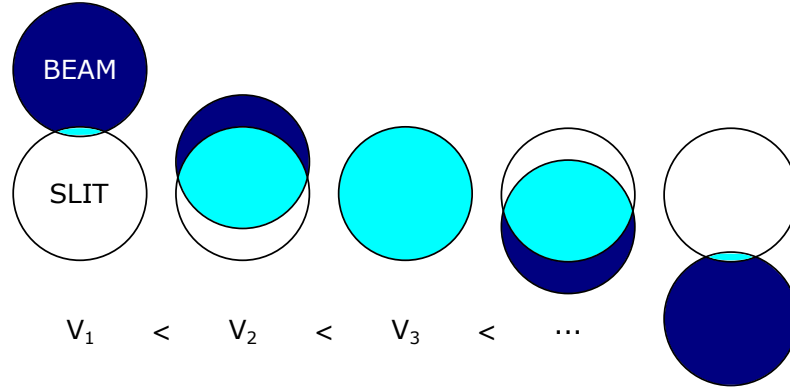


Figure 3.5: Schematic for the analysis of the beam profile. The light blue section gives the proportion of the beam that can pass the exit slit and impinges on the microchannel plate detector. V_1 , V_2 , etc. are the voltages applied between the electrodes of the analyser.

$$U = \frac{E_{kin}}{q_{ion} \cdot g} \quad , \quad g = \frac{C}{2 \cdot 4\pi\epsilon_0 R} = \left(\frac{r_2}{r_1} - \frac{r_1}{r_2} \right)^{-1} \quad . \quad (3.8)$$

The entrance aperture cuts the incoming beam such that its cross section is disk-shaped when it enters the field region. The focusing properties of the spherical sector analyser are such that the projection of the beam onto the exit aperture will again be close to a disk-shape. Thus geometrically, the part of the beam that passes the exit aperture to impinge on the microchannel plate detector is given by sliding a disk (the beam) across a circular hole (the exit aperture) and calculating the overlap of the two. This principle is depicted in Figure 3.5 where the proportion of the beam that can pass the exit slit for each voltage is given by calculating the light blue area. Obviously, the central trajectory gives the voltage where both disks are concentric to each other, while for too low voltages, the beam is above and for too low voltages the beam is below the exit aperture.

The width of the peak is obtained by calculating the energy resolution of the analyser, which is given by the full width at half maximum

$$\frac{\Delta E}{E} = \frac{\omega}{R(1 - \cos(\Phi)) + L \sin(\Phi)} \quad (3.9)$$

for spherical sector analysers [55], where Φ is the angle subtended by the analyser, R is the pass radius, L is the distance from the end of the sector field to the centre of the exit aperture and ω is the aperture diameter. To relate this energy resolution with the full width of the peak, it is necessary to look at the shape of the spectrometer function. Figure 3.6 shows a simulated peak overlaid with the function described above. The shape is very close to a triangle, so the full width can be approximately obtained by multiplying the energy resolution of the analyser by a factor of 2.

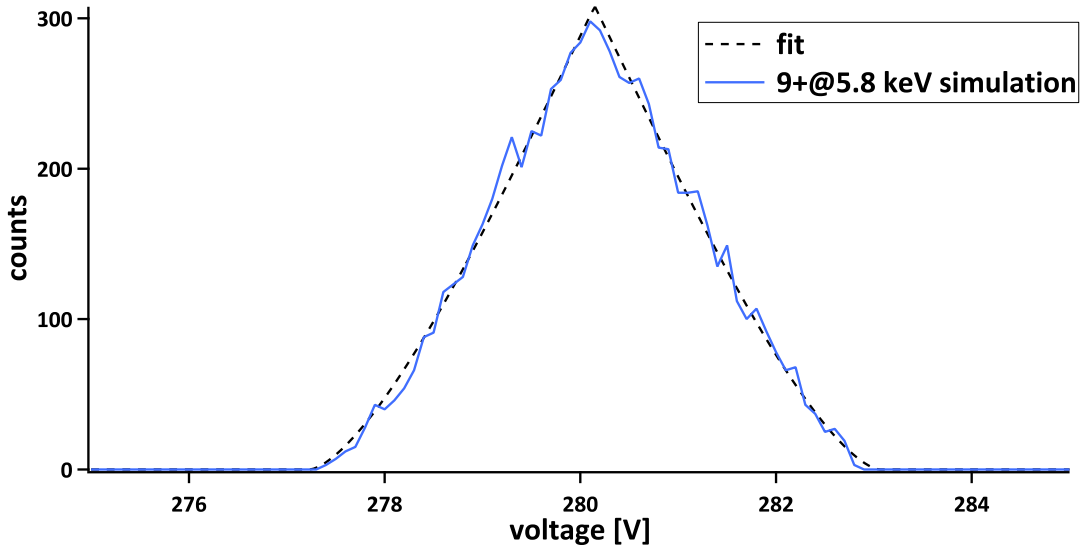


Figure 3.6: Simulated peak plus fit. Due to the mesh that SIMION uses for the ion trajectory calculations, the width of the simulated peaks is slightly wider than the original ones.

Influences like a tilt of the analyser can lead to a deviation of the peak shape from the nearly triangular shape and the formation of a plateau in the peaks, see Section 3.3.2. This change of the peak shape results from different diameters of the two disks in Figure 3.5. The implementation of this behaviour into the evaluation program is described in Section 3.4.

For completion it should be noted that a strongly divergent beam leads to asymmetric peaks, although due to the properties of the setup this should not be relevant for the measurements described in this work.

3.3.2 Angular shift of the peaks

Since the primary peak position in a spectrum is used to determine the mean energy of the ion beam, it is important to identify the influences apart from the kinetic energy that might evoke a shift of the peak positions.

One source that is easy to identify is a tilt of the analyser entrance relative to the beam. The coordinate system that will be referenced to is given in Figure 3.4.

When the beam is tilted in x-direction relative to the normal to the entrance slit, the beam position stays the same while the amplitude of the profile decreases, see Figure 3.7a. This can be attributed to the lens acting as a collimator cutting away more and more of the beam as the angle increases, see Figure 3.7b.

When the beam is tilted in y-direction, a shift of the peaks position can be observed. Figure 3.8 shows simulated peaks for different tilting angles. (+) means a tilt towards the inner electrode, (-) means a tilt towards the outer electrode.

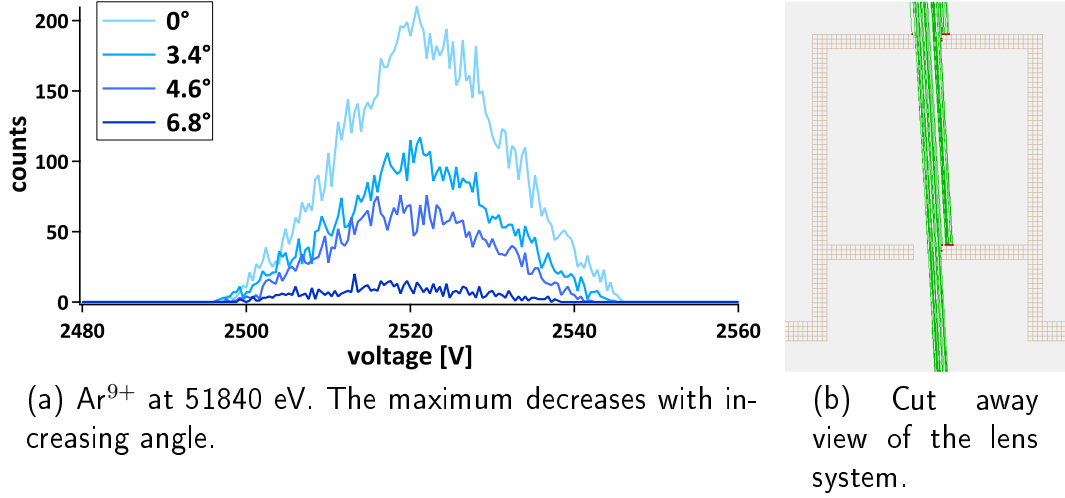


Figure 3.7: (a): Simulated peaks for a tilting of the beam in x-direction. The position stays the same while the amplitude decreases. (b): SIMION model of the lens system in front of the entrance slit. The lens system cuts away a portion of the beam, leading to the decrease of the measured beam intensity.

A tilt in the $+y$ -direction shifts the peaks to higher voltages while one in the $-y$ -direction does the opposite. This can be attributed to the fact that, for tilted beam trajectories, the exit slit of the analyser does not lie in the analyser's focal plane any more. As the beam direction diverges further from the normal, a plateau forms in the peak shape. Another effect that arises from an angle between the beam direction and the analyser entrance slit is that the peak width decreases with the absolute value of the tilting angle.

Figure 3.9a and Figure 3.9b show the peak shift (peak position at 0° - peak position at α°) plotted over the angle together with a quadratic fit to the data for different analyser voltage regimes. The parameters from the quadratic fit $U(\alpha) = A(\alpha - \alpha_0)^2 + C$ to the positional shift with respect to the entrance angle can be used to find a general expression for $U(\alpha)$:

$$U(\alpha) = U_0 * (1 + s \cdot [(\alpha - \alpha_0)^2 - \alpha_0^2]) \quad . \quad (3.10)$$

Here, $\alpha_0 \approx 3.1$ is the position of the maximum of the curve and $s \approx \frac{A}{C} \approx 2.8 \cdot 10^{-4}$. Since deviations from the simulated behaviour might occur in the real setup, this curve can only serve for qualitative analysis.

In Figure 3.9c, the decrease of the peak width with the angle can be seen. Both, the size of the peak widths and the positional shift, only depend on the pass voltage of the analyser, thus on a given $\frac{E_{kin}}{q}$ -ratio. Figure 3.9d displays the change of the amplitude with the tilting angle in y-direction.

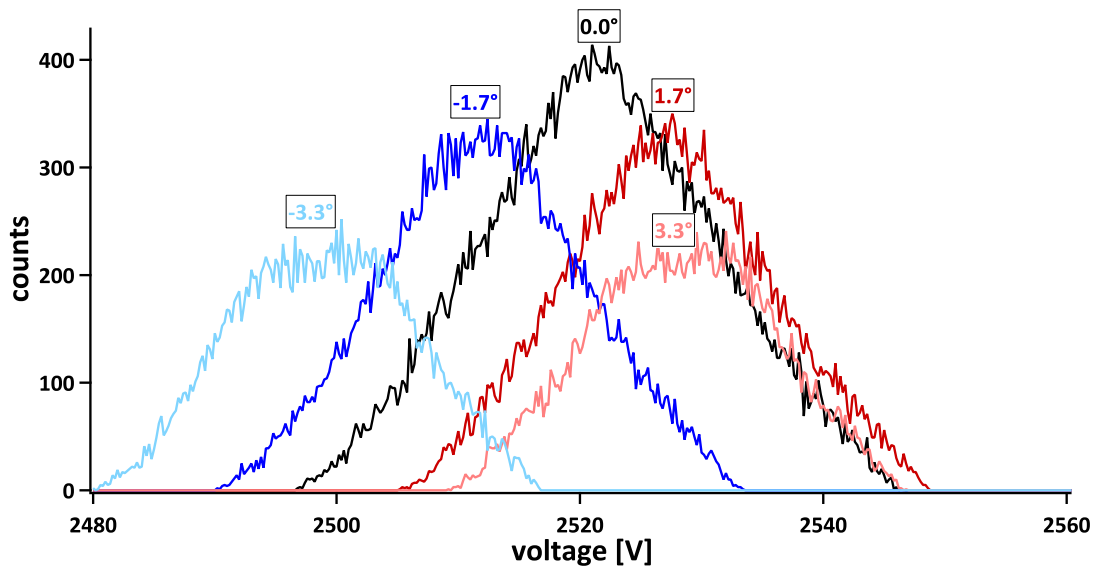


Figure 3.8: Peak shifts due to the angle between the beam and the normal to the analyser entrance slit. (+) means tilt towards the inner electrode, (-) towards the outer electrode.

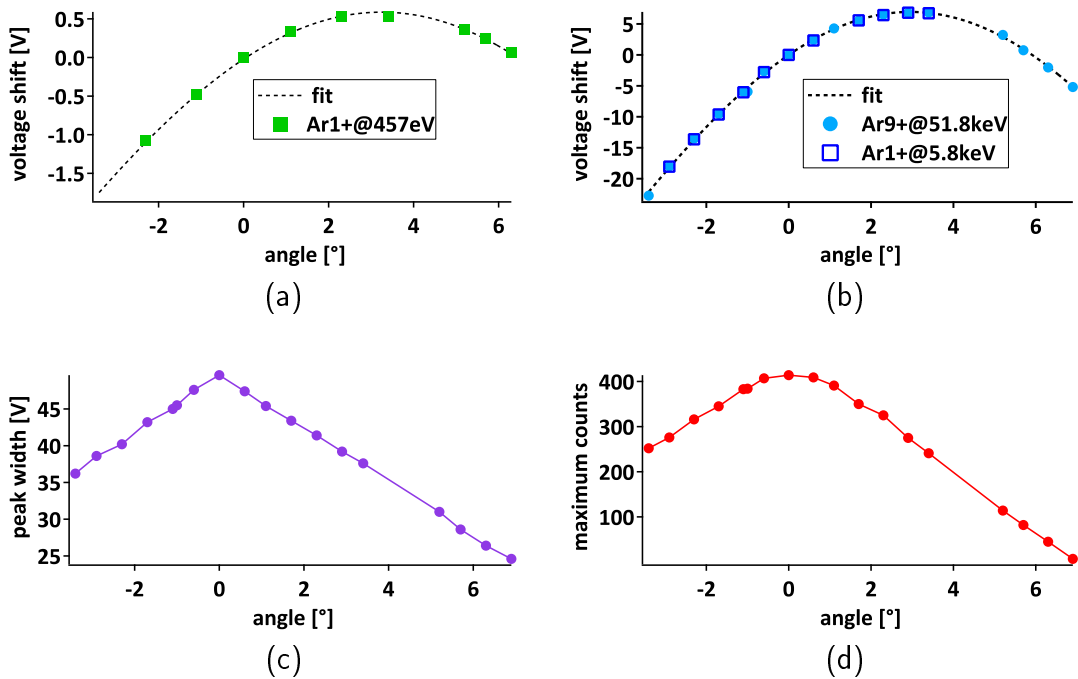


Figure 3.9: Changes of the peak properties with a tilting angle of the analyser in y-direction, where (+) means tilt towards the inner and (-) towards the outer electrode. (a),(b): Shift of the position of the peak maximum for ions with an analyser pass voltage of 280 V (a) and 2522 V (b). The dashed line is a quadratic fit to the data. (c): change of the peak width with the angle for ions with an analyser pass voltage of 2522 V. (d): change of the maximum count rate with the angle.

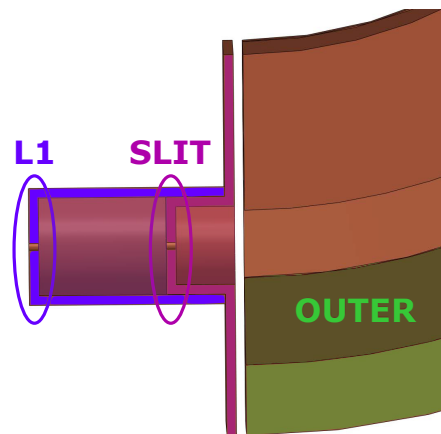


Figure 3.10: Close-up of the entrance region of the analyser. L1 (violet), SLIT (pink) and OUTER (green) can be connected to monitor the current intensities during adjustment of the analyser position.

3.4 Measurement procedure

In the following, the measurement procedure and the initial beam adjustment will be described.

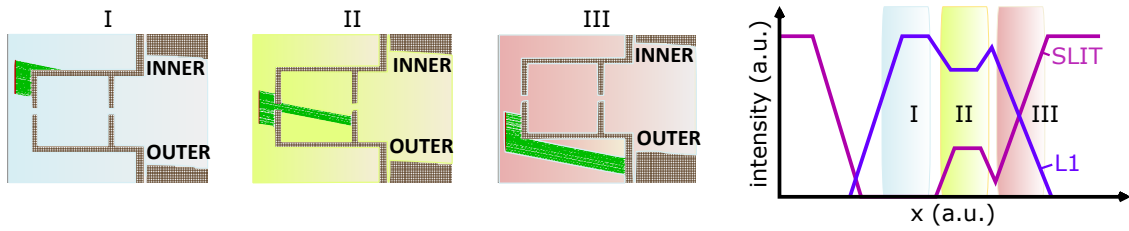
The first thing that is done when starting a measurement is to find the right operating parameters for the ion source that allow for a stable operation of the system throughout the recording of an entire spectrum. During this start-up procedure, the beam is monitored using a Faraday cup that can be inserted at the entrance of the beam line.

An important part of the measurements is given by guiding the beam through all the elements of the beamline, which is why the procedure will be discussed in this section.

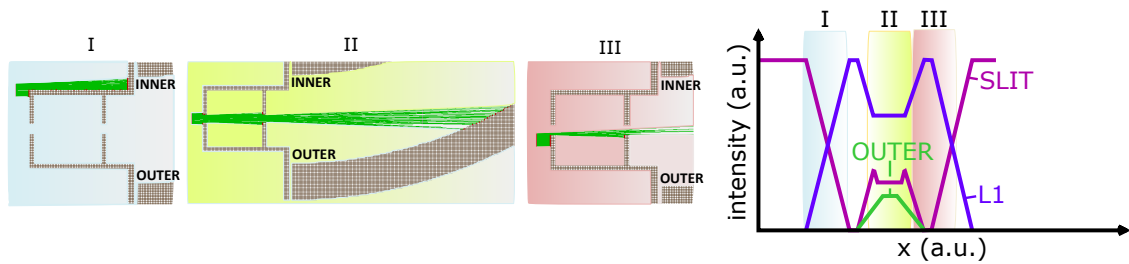
Figure 2.3 shows the collimator at the entrance of the beamline. By reading out the currents, which are in the order of some nA on the first aperture, on the different apertures and using the deflection plates, the beam can be guided through the ion optical system until the current is measured on the aperture of the target holder.

After that, L1, SLIT and OUTER (see Figure 3.10) can be connected to pico-amperemeters for further adjustments to the beam and electrostatic analyser position. Because of the three-element-lens at the entrance of the analyser which acts as a collimator, only fairly small angles between the beam and the lens will allow the beam to enter. By analysing the intensity profile of the measured currents on L1, SLIT and OUTER when moving the analyser in a direction normal to the beam, parallel alignment can be established.

The situation when the beam is tilted relative to the lens system of the analyser



(a) Tilted beam incidence.



(b) Straight beam incidence.

Figure 3.11: Intensity profile measured on the electrodes in the entrance region of the electrostatic analyser under (a) tilted and (b) straight incidence of the beam (green). For details see text.

is shown in Figure 3.11a. Moving the analyser up towards the beam, the following intensity profile is seen on the pico-amperemeters:

- 0** We start from a position where the entire beam current is collected on SLIT.
- I** Moving upwards, the current on SLIT decreases until all of it is measured on L1.
- II** Current will be measured on L1 and on SLIT without a signal on OUTER.
- III** The current on SLIT decreases, the one on L1 increases but after very little distance, the current on SLIT will rise again.

When observing this pattern we know that the beam is coming from above relative to the lens and the analyser has to be tilted upwards. An equivalent pattern obviously applies to the other tilting direction.

Only when the beam and the lens are aligned, an intensity profile as given in Figure 3.11b will be observed:

- I** The current intensity is distributed between SLIT and L1.
- II** Now the beam, SLIT and L1 are concentric and current is measured on the outer electrode.
- III** The currents on SLIT and on OUTER will almost simultaneously disappear when the analyser is moved further up.

Once the beam is guided through and current is measured on the outer electrode of the electrostatic analyser, the electrodes are reconnected to the voltage supply and the Elektra_Optimise.vi that is part of the LabVIEW project described in Section 2.1.2 can be taken into operation. A voltage is applied to the microchannel plate detectors by gradually increasing the voltage of the $-HV$ -control to 2100 V. Once the detector is operational, the potential between the electrodes is set to the pass voltage for the given $\frac{E_{kin}}{q}$ value of the beam. Now the signal can be monitored by the live graph in the program and the parameters and the alignment of the beam are adjusted.

After the beam is optimised, the Elektra_Main.vi is used to take an energy and charge loss spectrum.

3.5 Evaluation

As described in Section 3.3, the experimental peaks are given by a convolution of the spectrometer function with the energy distribution of the incoming ions. So finding a good fit to the energy and charge loss peaks of the spectra involves finding the appropriate energy distribution and working out the correct spectrometer function.

The primary peak together with the peaks displaying little charge loss will hardly show any straggling, thus they can be fitted using a Gaussian distribution.

In 1944, Landau found a solution to the energy loss distribution of particles traversing thin targets [56, 57], which seems apt for our type of experiment. His solution does not have a closed expression and Moyal deduced an analytic approximation to it that underestimates the tail but can be used to fit the peaks obtained in this experiment [58]. Since the measured spectra are plotted over the energy and not the energy loss, the width σ of the original Moyal distribution has to be replaced by $-\sigma$ to obtain:

$$f(x) = \frac{1}{\sqrt{2\pi\sigma}} \exp\left(-\frac{1}{2}e^{\frac{x-\mu}{\sigma}} + \frac{x-\mu}{2\sigma}\right) \quad , \quad (3.11)$$

where μ is the location parameter of the distribution. The mean of this distribution is given by

$$\bar{x} = \mu - \sigma(\gamma + \ln(2)) \quad , \quad (3.12)$$

where again σ has been replaced by $-\sigma$ and $\gamma \approx 0.57721$ is the Euler's constant.

Even though it does not have a simple analytic expression, the spectrometer function for the spherical sector analyser relevant for the ELEKTRA setup can be calculated following the considerations given in Section 3.3. The spectrometer function of the cylindrical sector analyser used in the setup at the HZDR is given by a box.

The above considerations were used to develop an evaluation program written in

python of which the basic structure has been designed by Magdalena Kralik [59]. For clarification, the implemented functions will first be discussed before covering the evaluation procedure.

The spectrometer function relevant for the ELEKTRA setup named above is implemented into the program with two scaling factors. Looking at the SIMION simulations, we can see that the peak shape as well as the peak width change with the angle between the beam and the normal to the entrance slit. To be able to adapt to those changes, two scaling parameters are inserted into the spectrometer function. On the one hand there is the **scale** parameter, which is a measure for the width of the plateau of the peaks. When we consider the area covered by two disks of different size, we will have an overlap region where the transmission is solely given by the area of the smaller disk. The ratio of the bigger disk radius to the smaller one defines **scale**. Figure 3.12 shows the dependence of the peak shape on this parameter.

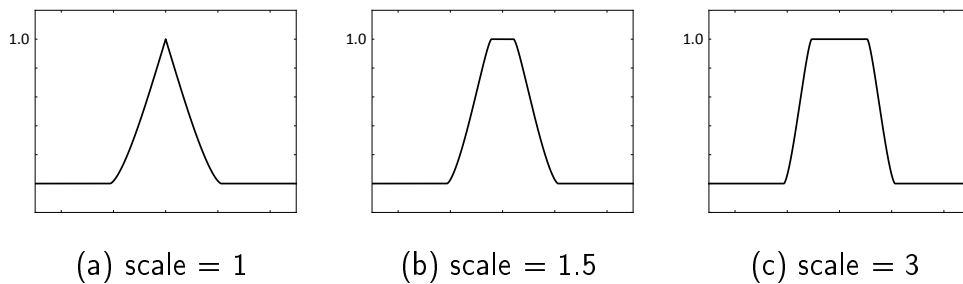


Figure 3.12: Effect of the scale parameter on the peak shapes. A larger scale parameter yields a larger plateau.

On the other hand there is the **fullwidth** parameter, which connects the full width at half maximum with the full width of the peak, with a default value of 2. The final fit function to the peaks is obtained by convolving this spectrometer function with a Gaussian (little charge loss) or the Moyal function (greater charge loss).

It should be noted that for the box function as well as for the spherical sector analyser spectrometer function plotted above, the correction to the integrals from the convolution scales with $\frac{1}{q}$.

The program now first determines the position and width of the first peak by fitting it using a non-linear least squares method. For including the distribution of the initial energy, the width of the primary Gaussian can be set before starting the program. Then, a plot showing the spectrum and the supposed positions of the peaks with a given ion source extraction voltage are shown and one can choose to insert offsets of the analyser voltage and the extraction voltage to adapt their

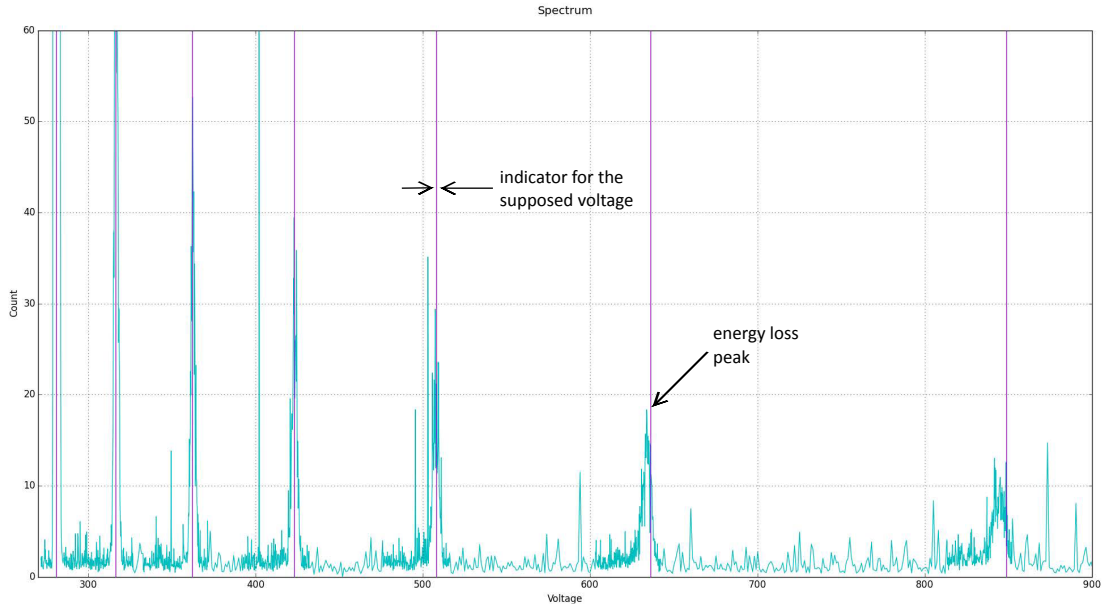


Figure 3.13: Spectrum during evaluation. The purple lines indicate the voltages where the peaks should be positioned according to the initial beam energy and the charge state. The first peaks are symmetric while the high charge loss peaks clearly exhibit straggling.

positions, see Figure 3.13. The vertical lines which represent the supposed positions of the peaks with a charge state q_{out} are shifted according to:

$$U_0 = \frac{(U_{SOURCE} + U_{SO}) \cdot q_{in}}{q_{out} \cdot g} + U_{AO} \quad , \quad (3.13)$$

where U_{SOURCE} is the source voltage, U_{SO} is the source offset voltage, U_{AO} is the offset of the analyser's voltage supply and q_{in} is the initial charge state of the ions.

Once the offsets are chosen, the peaks can be selected by clicking left and right of the peak and will then be fitted. The energy loss is determined by subtracting the mean of the fit from the calculated peak position U_0 . The total abundance of ions in a certain charge state is calculated by integrating over the deconvolved function (Gaussian or Moyal respectively) in order to avoid an overestimation due to an increasing spectrometer function width with decreasing exit charge state. A function that includes an angular shift according to Equation 3.10 was included as well.

3.5.1 Uncertainty estimation of the energy loss

Based on the considerations in Chapter 3, the uncertainty of the measured energy loss can be estimated. Assuming good alignment of the beam and the analyser, the two sources contributing to the uncertainty are:

- The uncertainty of the analyser voltage measurement.
- The uncertainty of the fit to the data.

Using the relation between the analyser voltage and the energy $E = g \cdot q \cdot U$ and the fact that the errors are uncorrelated we obtain as error for the i^{th} peak

$$\Delta E_i = g \cdot q \cdot \sqrt{(\Delta U_{analyser})^2 + (\Delta U_{fit})^2} \quad . \quad (3.14)$$

In the case of a symmetric, e.g. the Gaussian, distribution, $(\Delta U_{fit}) = \Delta\mu$, where μ is the position parameter. For the Moyal distribution, the uncertainty of the fit is given by $(\Delta U_{fit}) = \sqrt{(\Delta\mu)^2 + (\gamma + \ln(2))^2 \cdot \Delta\sigma^2}$. Taking the voltage readout of the analyser as the reference, $\Delta U_{analyser}$ is given by $\sqrt{2 \cdot (1.2 + 10^{-4} \cdot \frac{\mu}{2})^2}$. The energy loss E_{loss} is calculated by the difference between the initial beam energy and the mean of the fitted peak $E_{loss} = E_0 - E_i$, thus the error in the energy loss determination ΔE_{loss} is

$$\Delta E_{loss} = \sqrt{\Delta E_0^2 + \Delta E_i^2} \quad . \quad (3.15)$$

4 Results

4.1 Discussion of the setup

4.1.1 Spectra

As an example, Figure 4.1 shows a typical spectrum recorded in transmission measurements. It was taken for Ar^{9+} ions at $E_{kin} = 17.3$ keV after transmission through a CNM target. Figures 4.2a and 4.2b display the original data (pink) with the corresponding fit function (black), which is a convolution of the spectrometer function with a Gaussian for the first peaks of the spectrum and with a Moyal distribution for the peaks at large charge loss, as described in detail in Section 3.5. The fit is in excellent agreement with the data, supporting the spectrometer function chosen for the evaluation.

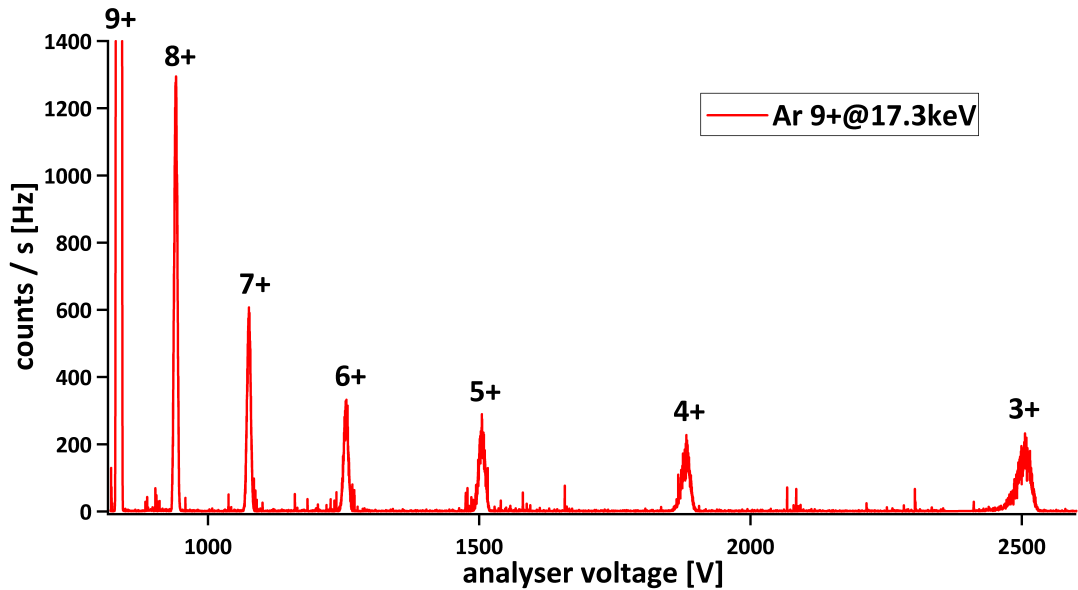


Figure 4.1: Typical spectrum recorded with the ELEKTRA-setup. Here an Ar^{9+} spectrum taken at $E_{kin} = 17.3$ keV after transmission through a CNM target is shown.

In order to obtain a good resolution of the low charge states it is necessary to extract high ion fluencies from the source. This will lead to a reduction of the counting efficiency of the detection system for the primary peak, since ion

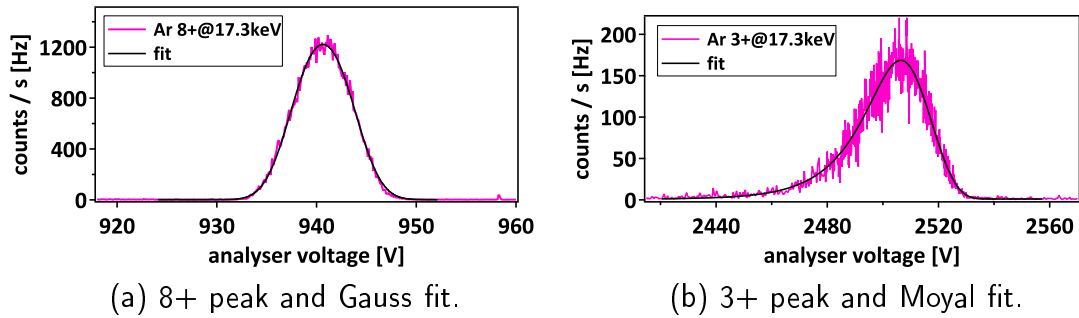


Figure 4.2: Original data and fit. A convolution of the spectrometer function with a Gaussian gives the fit to the low charge loss peaks (a), while a Moyal distribution is used for the high charge loss peaks (b).

impacts on the multichannel plate surface in rapid temporal succession will be counted as one signal. Hence for high primary count rates it is necessary to extract the spectrometer function for the fits from the second peak. Figure 4.3 shows a spectrum taken without a target at a high primary count rate of 200 kHz. Charge exchange with residual gas leads to the formation of a second peak which is a factor 300 smaller than the 9+ peak, whereas the second peak measured after transmission through the CNM is typically only one order of magnitude smaller than the primary. The peak left of the primary and the plateau left of the 8+ peak can be attributed to the primary peak hitting the outer or the inner electrode respectively and then being reflected onto the detector. Peak height analysis of the left peak showed no clear separation of the pulse from the background.

4.1.2 Offset voltage

A source of systematic error to the evaluation of the spectra was determined to be an unknown offset in the analyser voltage. Figure 4.4 shows the effect of different analyser offset values on the energy loss vs. charge loss curves. It is clear that a careful determination of the offset is necessary for accurate energy loss evaluation. A possibility to extract the analyser offset voltage is to record the primary peak positions for ions with a fixed charge state, only varying the extraction voltage (kinetic energy) U_{SOURCE} . The best fit to the data points with a positive source voltage offset evoked by the plasma potential U_{SO} and the analyser offset U_{AO} as free parameters will yield the analyser offset according to

$$U_0 = \frac{(U_{SOURCE} + U_{SO})}{g} + U_{AO} \quad . \quad (4.1)$$

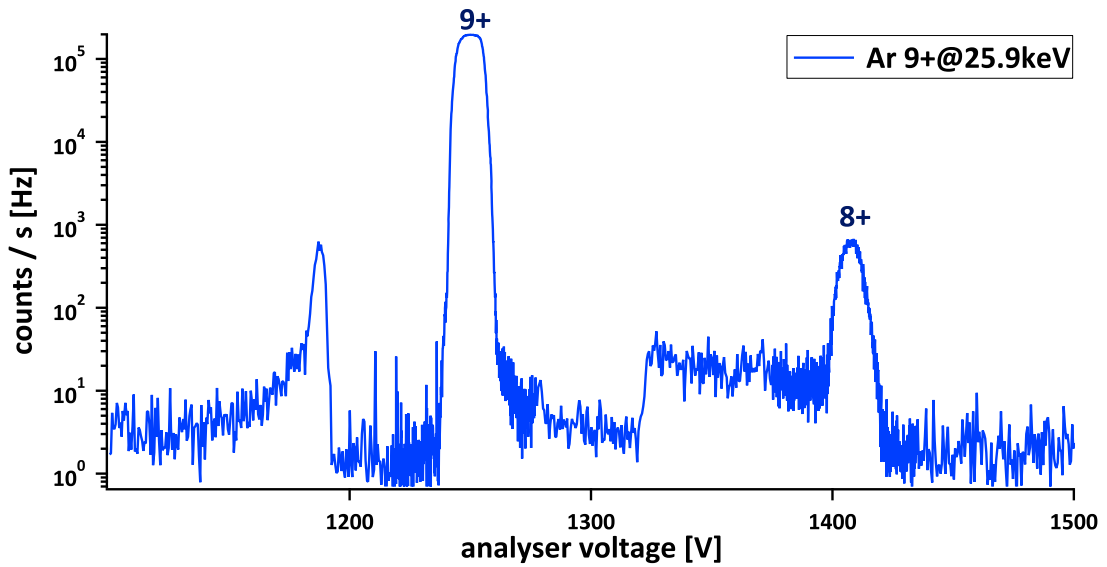


Figure 4.3: This charge exchange spectrum was taken without a target. A factor of 300 lies between 8+ peak and the primary peak. The peak on the left of the 9+ peak and the plateau on the right can be attributed to the primary peak hitting the outer or the inner electrode respectively and then being reflected onto the detector.

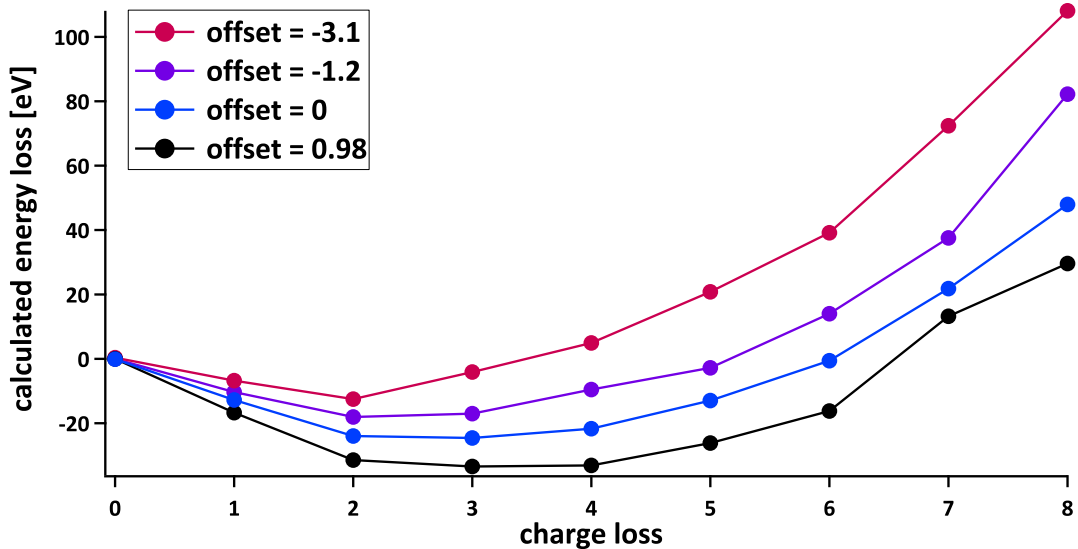


Figure 4.4: The effect of different analyser offsets on the calculated energy loss for an Ar^{9+} spectrum with $E_{\text{kin}} = 5.8$ keV. It is clear that a careful determination of the offset is crucial for energy loss measurements.

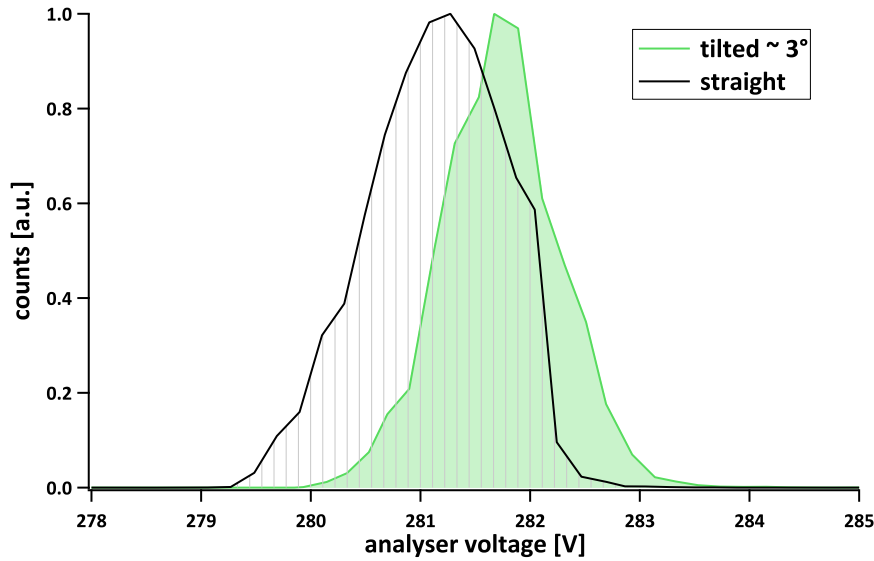


Figure 4.5: Measured peak shift due to changed alignment of the incoming beam and the analyser. The data was recorded with Ar^{7+} ions at $E_{kin} = 4.5$ keV before (green) and after (black) angular alignment.

4.1.3 Tilting angle of the analyser

The SIMION simulations described in Section 3.3 lead to the conclusion that a tilt of the analyser relative to the beam will on the one hand lead to the formation of a plateau in the spectrometer function and thus influence the fit of the peaks and hence the integrated intensity. On the other hand, and more importantly, it will lead to a shift of the peak positions. This effect increases for decreasing exit charge state. The shift cannot be corrected from the spectra computationally without detailed knowledge of the shift properties of the real apparatus which is why great care has to be taken in adjusting the analyser before performing measurements. An example of the shift when the angular alignment is adjusted can be seen in Figure 4.5. The change in the peak shape is no problem as long as the peaks can be fitted accurately since the integral over the spectrometer function scales with $\frac{1}{q}$, independent of the shape parameter.

4.2 Ar^{q+} on CNM

The focus of this thesis was to install and analyse the ELEKTRA setup and enable the evaluation of the recorded spectra, thus the results presented here have to be regarded as preliminary and should act as a proof of the functionality of the setup. The interaction of Argon ions in initial charge states between $q = 9$ and $q = 2$ and energies between 4.5 keV and 25.9 keV with CNM was investigated using the

ELEKTRA setup. The spectra discussed in the following were taken in forward direction. An analyser offset of 0 V was chosen for the evaluation in absence of knowledge of the real offset. Thus it has to be kept in mind that the results will be subject to systematic errors and only trends in the data can be discussed.

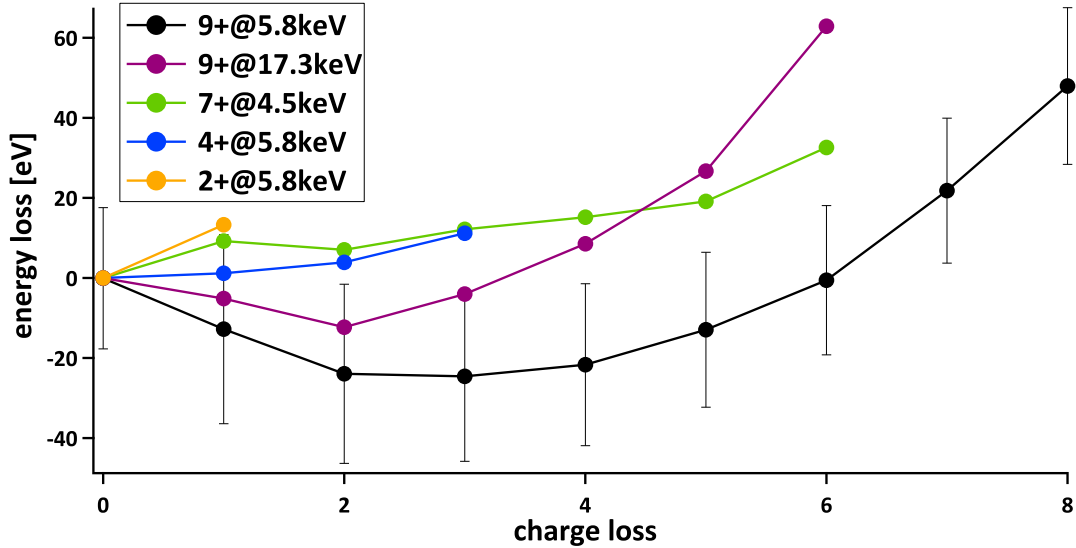


Figure 4.6: Energy loss vs. charge loss for different Ar-projectile charge states and different projectile energies after transmission through a carbon nano membrane. The error bars are only shown for one curve for clarity but are comparable for the other data sets.

Figure 4.6 shows energy loss of the projectiles plotted against the charge loss. The error bars have been omitted for all but one curve but are comparable for the other data sets. A striking feature is that the Ar^{9+} curves both cross the x-axis and turn towards negative energy loss values. Even though an energy gain due to image charge acceleration is possible this is not a valid explanation here, since those can be expected not to be exceeding a few eV, according to Equation 1.6. Looking at the analyser offset dependency of the energy loss shown in Figure 4.4 a negative offset needs to be chosen to obtain realistic energy loss values.

There is a clear correlation between energy loss and charge loss which has been observed earlier for Xe ions in higher charge states [10]. As well as that, the same charge loss leads to different energy losses depending on the residual charge. The tendency seems to be that for the same kinetic energy and the same charge loss the lower the exit charge state the higher the energy loss. It seems that the energy loss scales up with the energy brought into the collision.

Figure 4.7 shows the energy loss for ions of the same kinetic energies and a fixed exit charge state of $q_{\text{exit}} = 1$ as a function of the incident charge state. The solid lines are polynomial fits of second order to the data. The two curves have been obtained by using different analyser offset voltages, emphasising the importance of

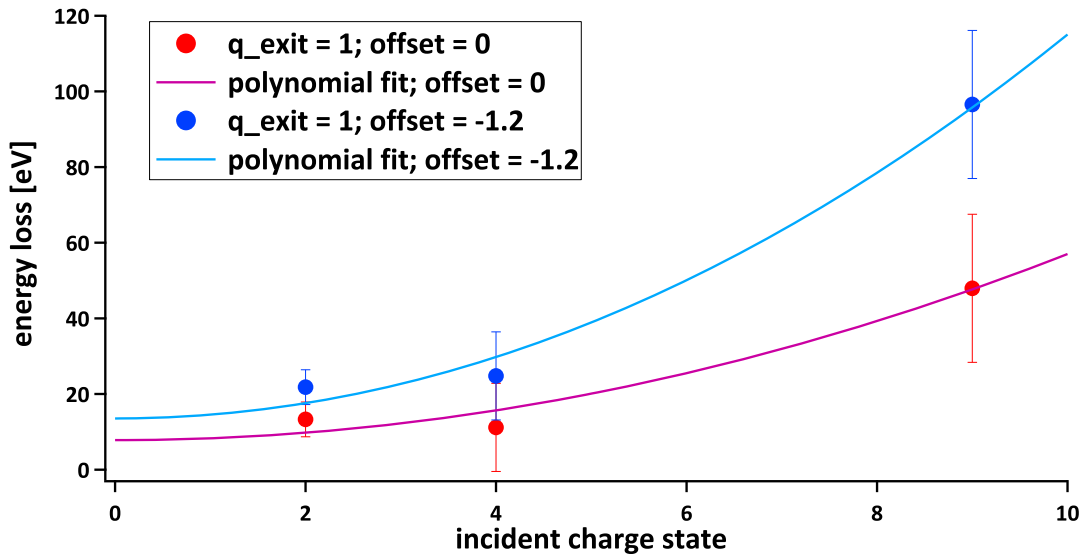


Figure 4.7: Energy loss vs. incident charge state for an exit charge state of $q_{\text{exit}} = 1$ and a kinetic energy of $E_{\text{kin}} = 5.8$ keV. The two different curves are obtained by using different analyser offsets. The markers are the original data while the solid line is a polynomial fit of second order to guide the eye.

a thorough determination thereof. A quadratic dependence of the energy loss on the incident charge state for highly charged ions was stated before in a theoretical treatment on the enhancement of nuclear stopping with projectile charge state by Biersack [40] and later the same dependence was measured by Wilhelm [10]. The offset of the solid line should extrapolate to the equilibrium stopping value of Argon ions on CNM.

The integrated normalised intensities over the exit charge state are shown in Figure 4.8. The normalisation was done with respect to the second peak of each spectrum since saturation effects of the detection system might lead to significant distortions of the data for high initial beam intensities. Since the beam intensity was only monitored for some of the spectra, an interpretation will be prone to errors. But the clear decrease of the amount of ions transmitted is preserved for the spectra where the beam intensity was measured before and after the measurement, which is why this trend can be assumed to be due to the interaction of the ions with the membrane and not due to a decrease of the ion beam current. This behaviour is different from the bimodal exit charge state distribution reported in [10] and [61]. The origin of the bimodal charge state distribution may be explained by the structure of the CNM, which is shown in Figure 4.9 and has been calculated using molecular dynamics simulations [60]. An ion impinging on such a membrane can either traverse a region of high (red marker) or low (green marker) atomic density, leading to close or distant collisions respectively. With the ELEKTRA setup, only ions with a divergence of $\pm 0.34^\circ$ can enter the analyser. For the measurements un-

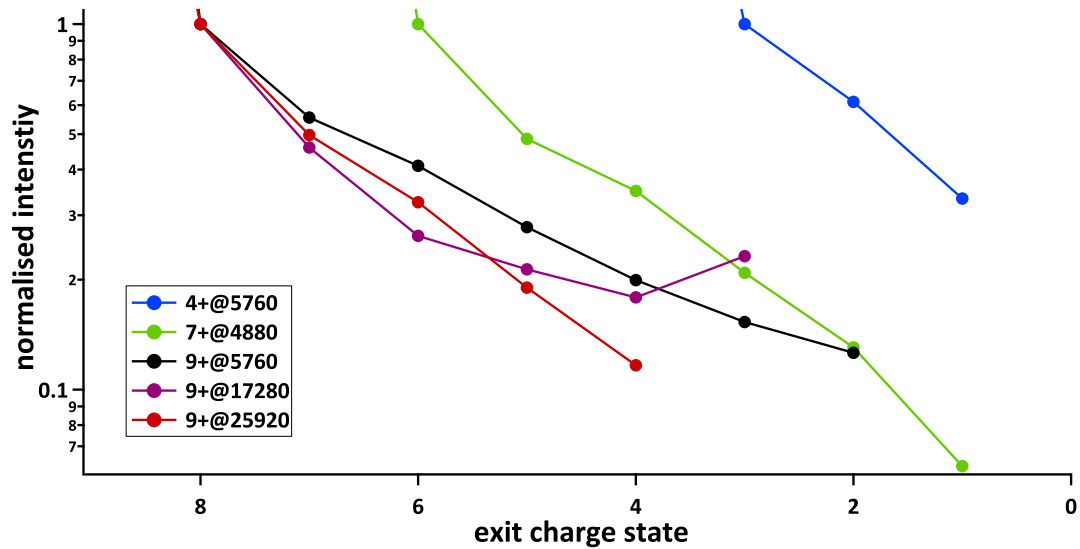


Figure 4.8: Deconvolved peak intensities normalised to the second peak vs. exit charge state. A clear decrease of intensity with decreasing exit charge state is visible.

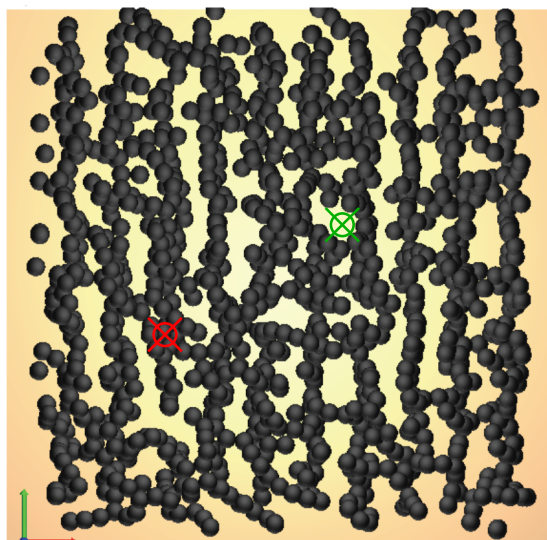


Figure 4.9: CNM structure calculated using molecular dynamics simulations. The red cross marks an area of high target atom density while the green cross marks one of low target atom density. Picture taken from [60].

der 0° described here, this imposes the restriction that only ions resulting from large impact parameter collisions are detected. Figure 4.10 visualises the dependence of the scattering angle on the impact parameter for elastic collisions of Ar with C, assuming a screened Coulomb potential given by Equation 1.15 as interaction potential. It can be seen that the energy loss contribution from elastic scattering is very small. The neutralisation mechanism for these ions is given by classical over the barrier capture of electrons, where each electron captured makes the process less likely thus leading to a decreasing intensity with charge loss, e.g. captured electrons. The low charge state distribution resulting from close collisions will occur in combination with scattering of projectiles under larger angles ($> 0.4^\circ$) and should be detected when rotating the analyser.

4.3 Xe^{q+} on single layer graphene

The first spectra of transmission measurements of highly charged Xe ions through free-standing single layer graphene recorded at the HZDR are presented together with possible explanations for the observations made therein. A fairly different behaviour from transmission through CNM can be expected for this target-projectile combination, since the largest possible impact parameter for graphene is when the ion passes through the middle of the target's hexagonal structure, see marker in Figure 4.11. Figure 4.12 shows a Xe^{32+} spectrum taken at $E_{\text{kin}} = 104.1$ keV. As expected, the high charge distribution that has been reported for transmission through CNM [10, 61] vanishes, reinforcing the idea that the high-q distribution results from large impact parameter collisions and the low-q distribution stems from close collisions. Another feature that has been observed is that the mean of the low-q distribution shifts towards higher charge loss for slower ions. This can be interpreted such that the interaction time limits the charge transfer to the projectile.

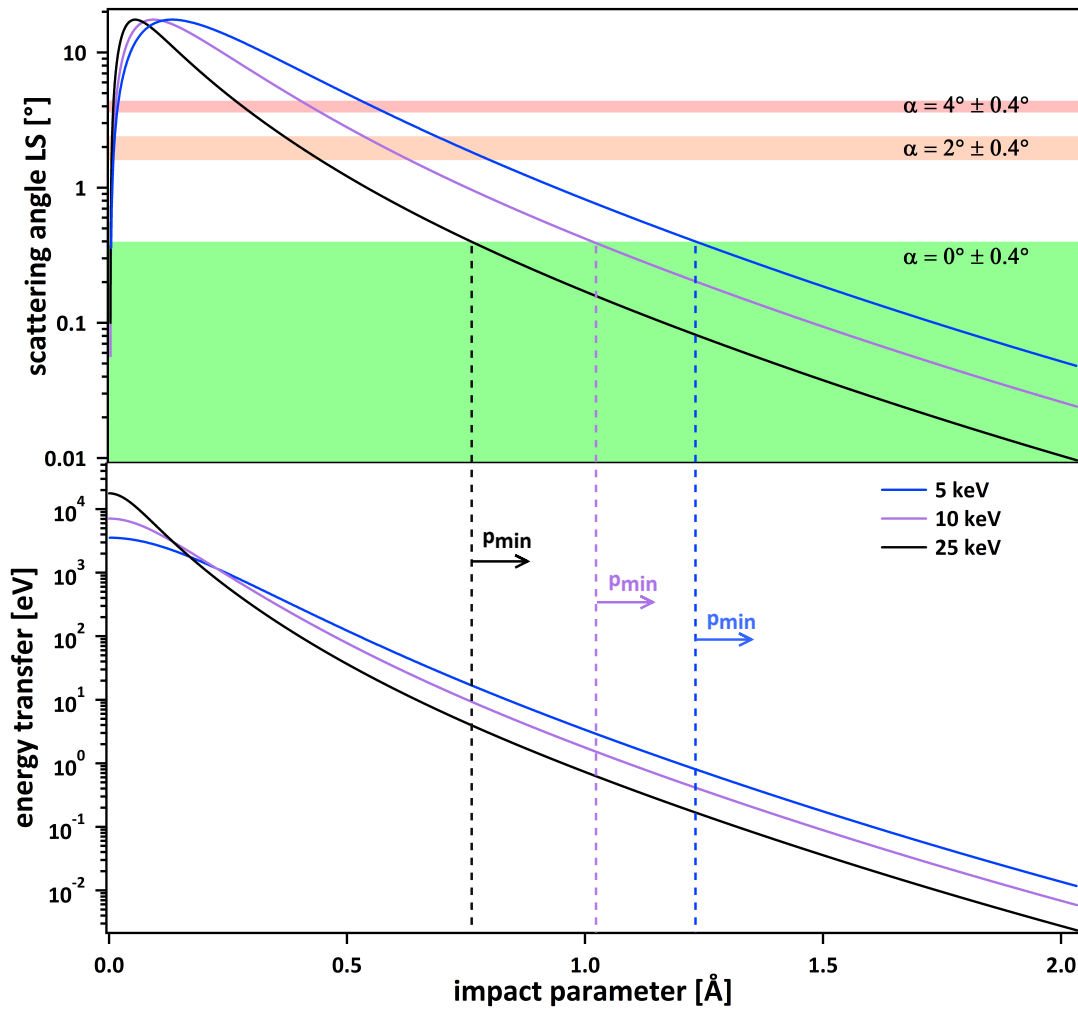


Figure 4.10: Elastic scattering angle and energy loss plotted over the impact parameter for Ar ions at different energies using the universal potential from Equation 1.15. Only ions interacting at large impact parameters (green area) can be seen under 0° tilting angle, which limits the energy loss that is measured to smaller values.

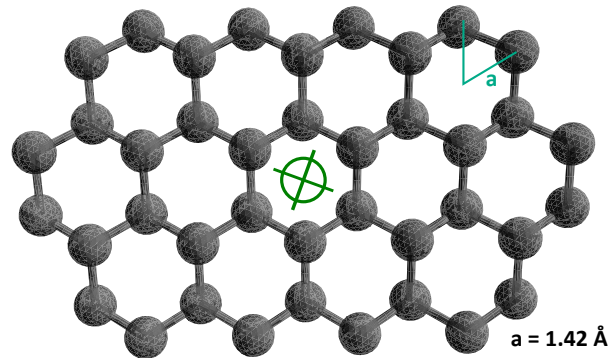


Figure 4.11: Graphene structure. The maximum impact parameter that is possible in a collision with graphene (marked by a green cross) is given by the distance a between two carbon atoms.

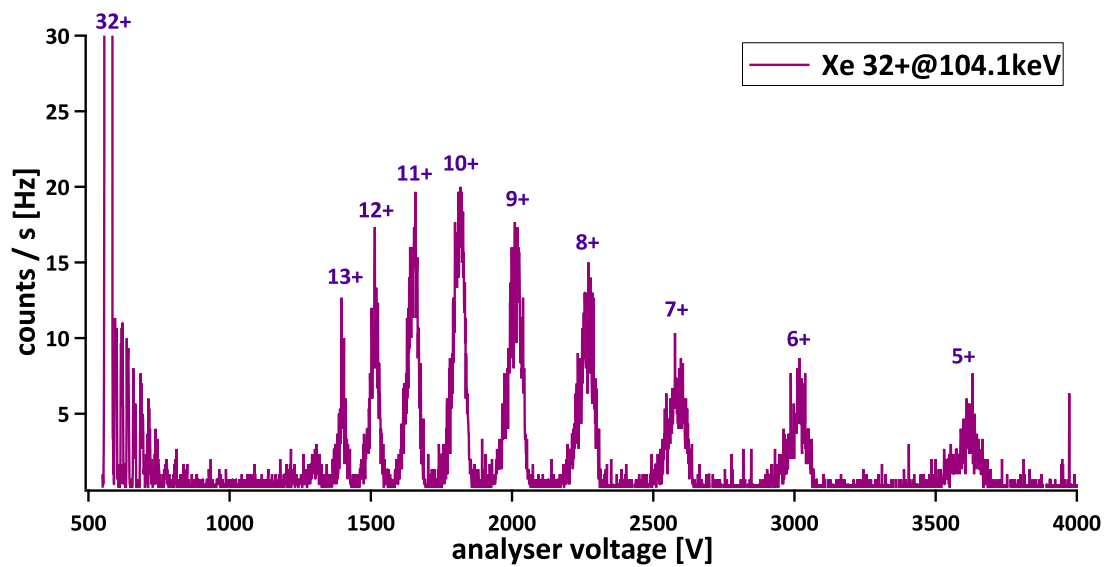


Figure 4.12: Spectrum taken for Xe^{32+} ions at $E_{kin} = 104.1 \text{ keV}$ after transmission through single layer graphene. The low charge loss distribution vanishes while the low- q distribution resulting from close collisions is preserved.

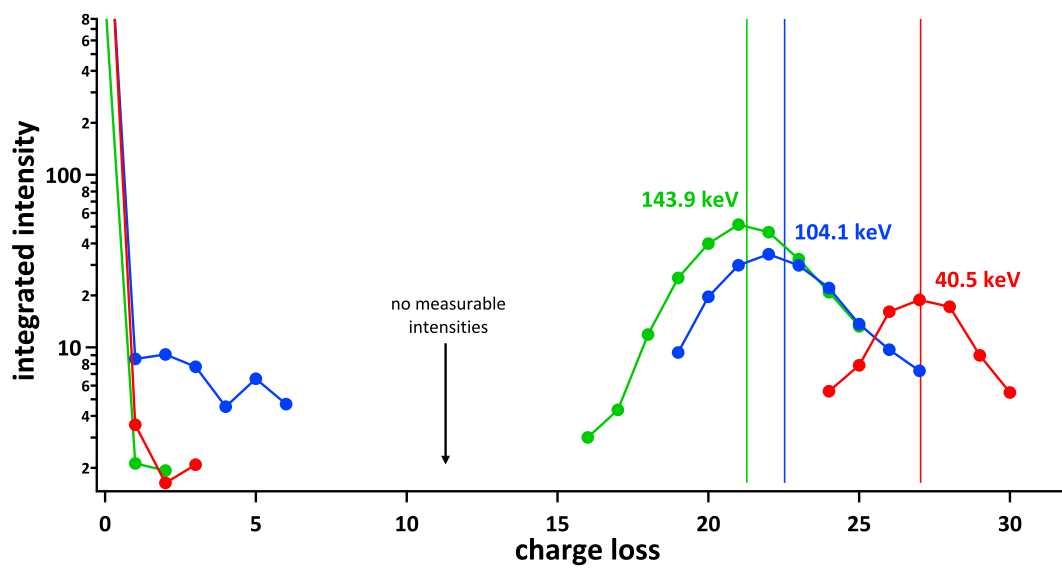


Figure 4.13: Integrated peak intensities on a logarithmic scale as a function of charge loss for Xe^{32+} ions of different energies after transmission through single layer graphene. It seems that the slower the ion, the more efficiently it can be neutralised.

5 Summary and outlook

5.1 Summary

A setup for transmission measurements through thin foils using an electrostatic spherical sector analyser was completed, put into operation and tested in the course of this thesis.

The completion included wiring of the setup and establishing the connection with all elements that can be computer-controlled. As well as that, a LabVIEW program for beam detection and optimisation and one for recording the data were created.

Simulations of beam trajectories inside the analyser were performed using the code SIMION 8.0. These simulations lead to a greater understanding of possible systematic errors inherent to the use of a spherical sector analyser. Theoretical considerations on the change of the shape of the transmitted beam due to the analyser geometry were made and compared with simulations. The results were included into the evaluation program for the spectra.

A first series of measurements with Ar as projectile ions and a carbon nano membrane target was performed with the ELEKTRA setup. So far, a lack of knowledge of the analyser offset makes quantitative evaluation of the energy loss impossible, but the energy loss clearly shows a strong dependence on the charge loss, in contrast to the predictions of conventional stopping theory. Systematic errors and too low statistics prohibited a direct measurement of a possible image charge acceleration of the projectiles in front of the target. The evaluation of the peak intensities shows a decrease towards lower charge states. Since only projectiles that are scattered from large impact parameters are registered during the measurements, this decrease can be explained by classical over the barrier capture of electrons, where multiple capture is unlikely.

First measurements of Xe ions on graphene were performed at the HZDR. The spectra show a distribution in the low charge state region. The mean value of this distribution moves towards lower q for lower energies, which can be explained by the longer interaction time for slower ions that facilitates neutralisation.

5.2 Outlook

Now that the functionality of the ELEKTRA setup has been shown it will be necessary to carefully determine the analyser offset before new spectra are recorded. Accurate alignment of the beam and analyser position as well as a regular monitoring of the beam will be included into the measurement process.

As a next step it will be interesting to perform measurements with the analyser tilted with respect to the beam direction, entering a regime of expected higher energy loss. The use of different projectile-target combinations might assist in developing a deeper understanding of the processes dominating pre-equilibrium stopping and the neutralisation of HCI in thin films.

The evaluation of the data obtained at the HZDR will give insight into the interaction of HCI with graphene. Supplemental measurements with Ar on graphene under straight and tilted incidence will also be performed with the ELEKTRA setup in the near future.

Additional TEM images of the graphene sheet after irradiation might give information on whether the charge, and thereby energy, deposition into the material give rise to damage formation, which is of interest for practical applications.

Possible improvements to the ELEKTRA setup include the installation of a monitor of the beam intensity during the measurements. Since the recording of a spectrum takes some time, fluctuations of the ion fluency will affect the integrals over the peaks and imposes restrictions on the accuracy of the measurements. For measurements with lower energy ions it might be necessary to remove the collimator in front of the target holder in order to increase the intensity of the beam. Further refinement of the setup should include neutral beam detection.

Currently a heatable target holder is being installed which will help to ensure that the target is not contaminated by water. Measurement on single, double and triple layer graphene could help to separate contributions from surface contaminations from the pure graphene-projectile interaction.

List of Figures

Figure 1.1	Highly charged ion in front of a surface.	3
Figure 1.2	Interaction potentials for an ion with $q = 10$ in front of a LiF surface.	5
Figure 1.3	Energy loss contributions from nuclear and electronic stopping.	7
Figure 2.1	The ion beam facility AUGUSTIN.	11
Figure 2.2	Experimental setup.	11
Figure 2.3	Cross section through the collimator and the ion optics. . .	12
Figure 2.4	Schematic of the electronics.	13
Figure 2.5	Channel layout of the voltage supply.	14
Figure 2.6	Block diagram of the sub-VI NHS_ReadWrite.vi.	16
Figure 2.7	Symbol and inputs/outputs of the voltage supply control program NHS_Commander.vi.	16
Figure 2.8	Block diagram of the counter readout.	17
Figure 2.9	Main screen of the program for beam optimisation.	18
Figure 2.10	Block diagram of the program for beam optimisation. . . .	18
Figure 2.11	Main screen of the measurement program.	19
Figure 2.12	Working principle of an EBIT.	21
Figure 2.13	Setup at the HZDR.	22
Figure 2.14	TEM image of the graphene sheet used in the experiments.	23
Figure 3.1	Views of a microchannel plate.	25
Figure 3.2	Shift of the pulse amplitude distribution with different incident ion charge state.	26
Figure 3.3	Shift of the pulse amplitude distribution with different detector voltages.	26
Figure 3.4	Simion model of the electrostatic analyser.	29
Figure 3.5	Schematic for the analysis of the beam profile.	30
Figure 3.6	SIMION-simulated peak plus fit.	31
Figure 3.7	Simulated peaks for a tilting of the beam in x-direction. . .	32
Figure 3.8	Peak shifts due to the angle between the beam and the normal to the analyser entrance slit.	33

Figure 3.9	Changes in the peak properties with a tilting angle of the analyser in y-direction.	33
Figure 3.10	Close-up of the entrance region of the analyser.	34
Figure 3.11	Analyser adjustment.	35
Figure 3.12	Peak shapes for different values of the scale parameter. . .	37
Figure 3.13	Spectrum during evaluation.	38
Figure 4.1	Typical spectrum recorded with the ELEKTRA-setup. . .	40
Figure 4.2	Original measured peaks and fit.	41
Figure 4.3	Charge exchange spectrum.	42
Figure 4.4	The effect of different analyser offsets on the calculated energy loss.	42
Figure 4.5	Measured peak shift due to changed alignment of the incoming beam and the analyser.	43
Figure 4.6	Energy loss vs. charge loss for different projectile charge states and different projectile energies.	44
Figure 4.7	Energy loss vs. incident charge state for an exit charge state of $q_{\text{exit}} = 1$ and a kinetic energy of $E_{\text{kin}} = 5.8$ keV.	45
Figure 4.8	Integrated normalised intensities vs. exit charge state. . .	46
Figure 4.9	CNM structure.	46
Figure 4.10	Elastic scattering angle and energy loss plotted over the impact parameter for Ar ions at different energies.	48
Figure 4.11	Graphene structure.	49
Figure 4.12	Spectrum taken for Xe^{32+} ions at $E_{\text{kin}} = 104.1$ keV after transmission through single layer graphene.	49
Figure 4.13	Integrated peak intensities vs. charge loss for Xe^{32+} ions on graphene.	50

List of Tables

2.1	SCPI commands used in communicating with the voltage supply. .	15
2.2	Operational modes of the NHS_Commander.vi.	15
3.1	Voltage calibration.	28

Bibliography

- [1] H. Kurz, F. Aumayr, H. Winter, D. Schneider, M. Briere, and J. McDonald. *Electron emission and image-charge acceleration for the impact of very highly charged ions on clean gold*. Physical Review A **49**, 4693 (1994).
- [2] F. Aumayr, H. Kurz, D. Schneider, M. Briere, J. McDonald, C. Cunningham, and H. Winter. *Emission of electrons from a clean gold surface induced by slow, very highly charged ions at the image charge acceleration limit*. Physical Review Letters **71**, 1943 (1993).
- [3] J. Burgdörfer, P. Lerner, and F. W. Meyer. *Above-surface neutralization of highly charged ions: The classical over-the-barrier model*. Physical Review A **44**, 5674 (1991).
- [4] J. Burgdörfer and F. Meyer. *Image acceleration of multiply charged ions by metallic surfaces*. Physical Review A **47**, R20 (1993).
- [5] L. Hägg, C. O. Reinhold, and J. Burgdörfer. *Above-surface neutralization of slow highly charged ions in front of ionic crystals*. Physical Review A **55**, 2097 (1997).
- [6] A. Geim and I. Grigorieva. *Van der Waals heterostructures*. Nature **499**, 419 (2013).
- [7] S. P. Adiga, C. Jin, L. A. Curtiss, N. A. Monteiro-Riviere, and R. J. Narayan. *Nanoporous membranes for medical and biological applications*. Wiley Interdisciplinary Reviews: Nanomedicine and Nanobiotechnology **1**, 568 (2009).
- [8] A. K. Geim and K. S. Novoselov. *The rise of graphene*. Nature Materials **6**, 183 (2007).
- [9] U. Bangert, W. Pierce, D. M. Kepaptsoglou, Q. Ramasse, R. Zan, M. H. Gass, J. A. V. den Berg, C. B. Boothroyd, J. Amani, and H. Hofsäss. *Ion Implantation of Graphene—Toward IC Compatible Technologies*. Nano Letters **13**, 4902 (2013). PMID: 24059439.
- [10] R. A. Wilhelm, E. Gruber, R. Ritter, R. Heller, S. Facsko, and F. Aumayr. *Charge Exchange and Energy Loss of Slow Highly Charged Ions in 1 nm Thick Carbon Nanomembranes*. Physical Review Letters **112**, 153201 (2014).

-
- [11] V. Smejkal. *Design of an electrostatic analyser setup for ion charge state and energy loss analysis after transmission through thin membranes*. Projektarbeit, TU Wien, Institute of Applied Physics (2015).
- [12] V. Smejkal, E. Gruber, R. Wilhelm, L. Brandl, R. Heller, S. Facsko, and F. Aumayr. *A setup for transmission measurements of low energy multiply charged ions through free-standing few atomic layer films*. Nuclear Instruments and Methods in Physics Research Section B: Beam Interactions with Materials and Atoms (submitted).
- [13] E. Gruber, R. A. Wilhelm, V. Smejkal, R. Heller, S. Facsko, and F. Aumayr. *Interaction of highly charged ions with carbon nano membranes*. Journal of Physics: Conference Series **635**, 012027 (2015).
- [14] R. A. Wilhelm, E. Gruber, V. Smejkal, S. Facsko, and F. Aumayr. *Charge State Dependent Energy Loss of Slow Ions - Part A: Experimental Results on Highly Charged Ion Transmission*. Physical Review A (submitted).
- [15] H. Ryufuku, K. Sasaki, and T. Watanabe. *Oscillatory behavior of charge transfer cross sections as a function of the charge of projectiles in low-energy collisions*. Physical Review A **21**, 745 (1980).
- [16] A. Bárány, G. Astner, H. Cederquist, H. Danared, S. Huldt, P. Hvelplund, A. Johnson, H. Knudsen, L. Liljeby, and K.-G. Rensfelt. *Absolute cross sections for multi-electron processes in low energy Ar $q+$ - Ar collisions: Comparison with theory*. Nuclear Instruments and Methods in Physics Research Section B: Beam Interactions with Materials and Atoms **9**, 397 (1985).
- [17] A. Niehaus. *A classical model for multiple-electron capture in slow collisions of highly charged ions with atoms*. Journal of Physics B: Atomic and Molecular Physics **19**, 2925 (1986).
- [18] J. J. Ducrée, F. Casali, and U. Thumm. *Extended classical over-barrier model for collisions of highly charged ions with conducting and insulating surfaces*. Physical Review A **57**, 338 (1998).
- [19] R. Heller. *Untersuchungen zur Wechselwirkung langsamer hochgeladener Ionen mit der Oberfläche von Ionenkristallen*. Ph.D. thesis, Technischen Universität Dresden, Fakultät Mathematik und Naturwissenschaften (2009).
- [20] P. M. Echenique, R. Ritchie, N. Barberan, and J. Inkson. *Semiclassical image potential at a solid surface*. Physical Review B **23**, 6486 (1981).
- [21] E. D. Palik. *Handbook of optical constants of solids*, vol. 3. Academic Press (1998).

- [22] J. Limburg, S. Schippers, R. Hoekstra, R. Morgenstern, H. Kurz, F. Aumayr, and H. Winter. *Do hollow atoms exist in front of an insulating LiF (100) surface?* Physical Review Letters **75**, 217 (1995).
- [23] C. Auth, T. Hecht, T. Igel, and H. Winter. *Image charge acceleration of multicharged ions in front of the surface of an insulator.* Physical Review Letters **74**, 5244 (1995).
- [24] J.-P. Briand, S. Thuriez, G. Giardino, G. Borsoni, V. Le Roux, M. Froment, M. Eddrief, C. De Villeneuve, B. D'Etat-Ban, and C. Sébenne. *Image acceleration of highly charged ions on metal, semiconductor, and insulator surfaces.* Physical Review A **55**, R2523 (1997).
- [25] J. F. Ziegler, M. D. Ziegler, and J. P. Biersack. *SRIM*. Cadence Design Systems (2008).
- [26] F. Aumayr, S. Facsko, A. S. El-Said, C. Trautmann, and M. Schleberger. *Single ion induced surface nanostructures: a comparison between slow highly charged and swift heavy ions.* Journal of Physics: Condensed Matter **23**, 393001 (2011).
- [27] N. Bohr. *II. On the theory of the decrease of velocity of moving electrified particles on passing through matter.* The London, Edinburgh, and Dublin Philosophical Magazine and Journal of Science **25**, 10 (1913).
- [28] J. Ziegler, J. Biersack, and U. Littmark. *The stopping and ranges of ions in solids, Vol. 1.* Pergamon Press (1985).
- [29] N. Bohr. *The penetration of atomic particles through matter.* Mat. Fys. Medd. Dan. Vid. Selsk. **18** (1948).
- [30] O. Firsov. *Calculation of atomic interaction potentials.* Zh. Eksp. Teor. Fiz **33**, 696 (1957).
- [31] J. Lindhard, V. Nielsen, and M. Scharff. *Approximation Method in Classical Scattering by Screened Coulomb Fields.* Mat. Fys. Medd. Dan. Vid. Selsk. **36** (1968).
- [32] G. Amsel, G. Battistig, and A. L'hoir. *Small angle multiple scattering of fast ions, physics, stochastic theory and numerical calculations.* Nuclear Instruments and Methods in Physics Research Section B: Beam Interactions with Materials and Atoms **201**, 325 (2003).
- [33] F. Bloch. *Zur Bremsung rasch bewegter Teilchen beim Durchgang durch Materie.* Annalen der Physik **408**, 285 (1933).

-
- [34] P. Sigmund. *Stopping of heavy ions: a theoretical approach*. 204. Springer Science & Business Media (2004).
- [35] O. Firsov. *A qualitative interpretation of the mean electron excitation energy in atomic collisions*. Journal of Experimental and Theoretical Physics (USSR) **36** (1959).
- [36] J. Lindhard and M. Scharff. *Energy dissipation by ions in the keV region*. Physical Review **124**, 128 (1961).
- [37] T. Schenkel, M. A. Briere, A. V. Barnes, A. V. Hamza, K. Bethge, H. Schmidt-Böcking, and D. H. Schneider. *Charge State Dependent Energy Loss of Slow Heavy Ions in Solids*. Physical Review Letters **79**, 2030 (1997).
- [38] T. Schenkel, M. A. Briere, H. Schmidt-Böcking, K. Bethge, and D. H. Schneider. *Electronic Sputtering of Thin Conductors by Neutralization of Slow Highly Charged Ions*. Physical Review Letters **78**, 2481 (1997).
- [39] T. Schenkel, A. Hamza, A. Barnes, and D. Schneider. *Interaction of slow, very highly charged ions with surfaces*. Progress in Surface Science **61**, 23 (1999).
- [40] J. Biersack. *The effect of high charge states on the stopping and ranges of ions in solids*. Nuclear Instruments and Methods in Physics Research Section B: Beam Interactions with Materials and Atoms **80**, 12 (1993).
- [41] E. Galutschek, R. Trassl, E. Salzborn, F. Aumayr, and H. Winter. *Compact 14.5 GHz all-permanent magnet ECRIS for experiments with slow multicharged ions*. Journal of Physics: Conference Series **58**, 395 (2007).
- [42] E. Galutschek. *Development of a 14.5 GHz All-Permanent Magnet Multicharged ECR Source for Remote Operation*. Ph.D. thesis, TU Wien (2005).
- [43] E. Gruber. *Ion Guiding Through Insulating Glass Capillaries*. Master's thesis, TU Wien, Institute of Applied Physics (2012).
- [44] A. Turchanin, A. Beyer, C. T. Nottbohm, X. Zhang, R. Stosch, A. Sologubenko, J. Mayer, P. Hinze, T. Weimann, and A. Gölzhäuser. *One nanometer thin carbon nanosheets with tunable conductivity and stiffness*. Advanced Materials **21**, 1233 (2009).
- [45] R. Wilhelm. *Wechselwirkung langsamer hochgeladener Ionen mit Ionenkristalloberflächen und ultradünnen Kohlenstoffmembranen*. Ph.D. thesis, Technische Universität Dresden (2014).

- [46] G. Zschornack, M. Kreller, V. Ovsyannikov, F. Grossman, U. Kentsch, M. Schmidt, F. Ullmann, and R. Heller. *Compact electron beam ion sources/traps: Review and prospects (invited) a*). Review of Scientific Instruments **79**, 02A703 (2008).
- [47] F. Currell and G. Fussmann. *Physics of electron beam ion traps and sources*. IEEE Transactions on Plasma Science **33**, 1763 (2005).
- [48] J. L. Wiza. *Microchannel plate detectors*. Nuclear Instruments and Methods **162**, 587 (1979).
- [49] O. H. W. Siegmund. *7. Amplifying and Position Sensitive Detectors*. Vacuum Ultraviolet Spectroscopy II. Series: Experimental Methods in the Physical Sciences **32**, 139 (1998).
- [50] Hamamatsu Photonics K.K. *Characteristics and Applications of Microchannel Plates* (2006).
- [51] J. Adams and B. W. Manley. *The Mechanism of Channel Electron Multiplication*. IEEE Transactions on Nuclear Science **13**, 88 (1966).
- [52] D. Rogers and R. F. Malina. *Optimization of the performance of a tandem microchannel plate detector as a function of interplate spacing and voltage*. Review of Scientific Instruments **53**, 1438 (1982).
- [53] A. G. Drentje. *Techniques and mechanisms applied in electron cyclotron resonance sources for highly charged ions*. Review of Scientific Instruments **74**, 2631 (2003).
- [54] I. Scientific Instrument Services. *SIMION. Industry standard charged particle optics simulation software*. <http://www.simion.com>. Accessed: 2015-07-23.
- [55] J. H. Moore, C. C. Davis, M. A. Coplan, and S. C. Greer. *Building scientific apparatus*. Cambridge University Press (2009).
- [56] L. Landau. *On the energy loss of fast particles by ionization*. Journal of Physics (USSR) **8**, 201 (1944).
- [57] P. Sigmund. *Particle Penetration and Radiation Effects*. Springer-Verlag Berlin Heidelberg (2006).
- [58] J. Moyal. *XXX. Theory of ionization fluctuations*. The London, Edinburgh, and Dublin Philosophical Magazine and Journal of Science **46**, 263 (1955).
- [59] M. Kralik. *Design of an evaluation program for energy and charge loss spectra*. Projektarbeit (unfinished), TU Wien, Institute of Applied Physics (2015).

-
- [60] A. Mrugalla and J. Schnack. *Classical molecular dynamics investigations of biphenyl-based carbon nanomembranes*. Beilstein Journal of Nanotechnology **5**, 865 (2014).
- [61] R. A. Wilhelm, E. Gruber, R. Ritter, R. Heller, A. Beyer, A. Turchanin, N. Klingner, R. Hübner, M. Stöger-Pollach, H. Vieker, G. Hlawacek, A. Götzhäuser, S. Facsko, and F. Aumayr. *Threshold and efficiency for perforation of 1 nm thick carbon nanomembranes with slow highly charged ions*. 2D Materials **2**, 035009 (2015).

*Ever tried. Ever failed. No matter.
Try again. Fail again. Fail better.*

- SAMUEL BECKETT

Danksagung

Am Ende meiner Diplomarbeit möchte ich noch all jenen gegenüber meinen Dank zum Ausdruck bringen, die wesentlich an ihrer Entstehung beteiligt waren.

Zuallererst geht mein Dank an Prof. Dr. Friedrich Aumayr, der mir tatkräftig geholfen hat, meinen Weg in das Thema zu finden und meinen Ideen geduldig gelauscht hat und immer wertvolle Anregungen in petto hatte. Er eröffnete mir zahlreichen Möglichkeiten, in die Welt des akademischen Arbeitens hineinzuschnuppern und ließ mir dabei große Selbstständigkeit. Seine offene und umgängliche Art tragen zu einem einmaligem Arbeitsgruppenklima bei.

Danke an die Mitarbeiter der Werkstatt, Herbert Schmidt und Rainer Gärtner, die aus manch utopischem Vorschlag einen umsetzbaren machten.

Danke auch an meine Kollegen und Kolleginnen in der Arbeitsgruppe, die mich mit besserer (Alexander Fuchs-Fuchs) und schlechterer (Florian Laggner) musikalischer Unterhaltung bei Messzeiten und auch sonst im Labor unterstützten. Ich danke Bernhard Berger, dass er mir mit seinem Know-How zum Zeichnen technischer Pläne zur Verfügung stand. Besonders Katharina Dobes danke ich für ihre ruhige Art, den wunderbaren Sprachhumor und die geisteswissenschaftliche Seele, du hast mir immer sehr gut getan.

Ganz besonderen Dank möchte ich meiner Betreuerin Elisabeth Gruber aussprechen, deren unglaubliche Zielstrebigkeit und Erfahrung im Labor mich sehr motiviert haben. Ihre gute Intuition, wo nach Fehlern zu suchen ist und die schnelle Umsetzung von Verbesserungen haben mich oft vor Irrwegen bewahrt. Du hast dir wahnsinnig viel Zeit dafür genommen, um mit mir zu diskutieren und mich nicht nur fachlich gut geleitet sondern hast mir auch in Zeiten, wo nichts zu funktionieren schien, als große Stütze gedient. Wir hatten sehr lustige Zeiten gemeinsam, im Labor bei nächtlichen Umbauaktionen und abseits der Uni und hast dazu beigetragen, die Zeit unvergesslich zu machen und eine tiefe Freundschaft zu knüpfen.

Ein großes Dankeschön geht auch an Julian, der mich mental beim Verfassen dieser Arbeit sehr unterstützt hat und mir mit unglaublicher Geduld, Liebe und seiner ruhigen Art half, einigermaßen effizient zu arbeiten. Durch dich habe ich die Zeit des Zusammenschreibens nicht als anstrengende, sondern als sehr schöne Zeit in Erinnerung. Danke, dass du mir gut zugesprochen hast und die erste Rohfassung so sorgfältig von Fehlern befreit hast!

Und - last but not least - will ich mich bei meinen Eltern bedanken. Ihr habt mich, ohne mir jemals Druck zu machen, mental wie finanziell mein gesamtes Studium unterstützt. Danke, dass ihr immer für mich da seid.